12-2017

Impacts of Distributions and Trajectories on Navigation Uncertainty Using Line-of-Sight Measurements to Known Landmarks in GPS-Denied Environments

Ryan D. Lamoreaux
Utah State University

IMPACTS OF DISTRIBUTIONS AND TRAJECTORIES ON NAVIGATION UNCERTAINTY USING LINE-OF-SIGHT MEASUREMENTS TO KNOWN LANDMARKS IN GPS-DENIED ENVIRONMENTS

by

Ryan D. Lamoreaux

A thesis submitted in partial fulfillment
of the requirements for the degree

of

MASTER OF SCIENCE

in

Electrical Engineering

Approved:

Rajnikant Sharma, Ph.D. Major Professor	Jacob Gunther, Ph.D. Committee Member
Todd Moon, Ph.D. Committee Member	Morgan Davidson, M.S. Committee Member

Mark R. McLellan, Ph.D
Vice President for Research and
Dean of the School of Graduate Studies

UTAH STATE UNIVERSITY
Logan, Utah

2017

ABSTRACT

Impacts of Distributions and Trajectories on Navigation Uncertainty Using Line-of-Sight Measurements to Known Landmarks in GPS-Denied Environments

by

Ryan D. Lamoreaux, Master of Science

Utah State University, 2017

Major Professor: Rajnikant Sharma, Ph.D.
Department: Electrical and Computer Engineering

To date, global positioning systems (GPS) occupy a crucial place in most navigation systems. Because reliable GPS is not universally available, navigation within GPS-denied environments is an area of deep interest in both military and civilian applications. Image-aided inertial navigation is one alternative navigational solution in GPS-denied environments. One form of image-aided navigation measures the bearing from the vehicle to a feature or landmark of known location using a monocular imager to deduce information about the vehicle's position and attitude. This work uncovers and explores several impacts of trajectories and landmark distributions on the navigation information gained from this type of aiding measurement. To do so, a modular system model and extended Kalman filter (EKF) are described and implemented. A quadrotor system model is first presented. This model is implemented and then used to produce sensor data for several trajectories of varying shape, altitude, and landmark density. Next, navigation data is produced by running the sensor data through an EKF. The data is plotted and examined to determine effects of each variable. These effects are then explained. Finally, an equation describing the quantity of information in each measurement is derived and related to the patterns seen in the data. The resulting equation is then used to explain selected patterns in the

data. Other uses of this equation are presented, including applications to path planning and landmark placement.

(84 pages)

PUBLIC ABSTRACT

Impacts of Distributions and Trajectories on Navigation Uncertainty Using Line-of-Sight Measurements to Known Landmarks in GPS-Denied Environments

Ryan D. Lamoreaux

Unmanned vehicles are increasingly common in our world today. Self-driving ground vehicles and unmanned aerial vehicles (UAVs) such as quadcopters have become the fastest growing area of automated vehicles research. These systems use three main processes to autonomously travel from one location to another: guidance, navigation, and controls (GNC). Guidance refers to the process of determining a desired path of travel or trajectory, affecting velocities and orientations. Examples of guidance activities include path planning and obstacle avoidance. Effective guidance decisions require knowledge of one's current location. Navigation systems typically answer questions such as: "Where am I? What is my orientation? How fast am I going?" Finally, the process is tied together when controls are implemented. Controls use navigation estimates (e.g., "Where I am now?") and the desired trajectory from guidance processes (e.g., "Where do I want to be?") to control the moving parts of the system to accomplish relevant goals.

Navigation in autonomous vehicles involves intelligently combining information from several sensors to produce accurate state estimations. To date, global positioning systems (GPS) occupy a crucial place in most navigation systems. However, GPS is not universally reliable. Even when available, GPS can be easily spoofed or jammed, rendering it useless. Thus, navigation within GPS-denied environments is an area of deep interest in both military and civilian applications. Image-aided inertial navigation is an alternative navigational solution in GPS-denied environments. One form of image-aided navigation measures the bearing from the vehicle to a feature or landmark of known location using a single lens imager, such as a camera, to deduce information about the vehicle's position and attitude.

This work uncovers and explores several of the impacts of trajectories and landmark distributions on the navigation information gained from this type of aiding measurement. To do so, a modular system model and extended Kalman filter (EKF) are described and implemented. A quadrotor system model is first presented. This model is implemented and then used to produce sensor data for several trajectories of varying shape, altitude, and landmark density. Next, navigation data is produced by running the sensor data through an EKF. The data is plotted and examined to determine effects of each variable. These effects are then explained. Finally, an equation describing the quantity of information in each measurement is derived and related to the patterns seen in the data. The resulting equation is then used to explain selected patterns in the data. Other uses of this equation are presented, including applications to path planning and landmark placement.

ACKNOWLEDGMENTS

I am grateful to Dr. Rajnikant Sharma for patiently guiding me through this work, even when his career moved him across the country before we even really began. I am also grateful to the rest of my committee members for their invaluable help in every step of this process. Several friends and coworkers at the Space Dynamics Laboratory in Logan, Utah, including Morgan Davidson, Randy Christensen, Keith Blonquist, Jonathan Haws, and Kori Moore were also encouraging, enabling and helpful. Most of all, I am grateful to my wife, Ashli, and our kids. They have been patient with me while I have worked diligently to finish everything up.

Ryan D. Lamoreaux

CONTENTS

LIST OF TABLES

Table Page

LIST OF FIGURES

MATH NOTATION

The following mathematical notation will apply to the rest of this work unless otherwise specified:

a	-	scalar variable, no hat or tilde indicates a "true" value
$\dot{a}$	-	the time-derivative of value a, or $\frac{\delta a}{\delta t}$
$\hat{a}$	-	estimated value of a
$\tilde{a}$	-	measured value of a
$\mathscr{A}$	-	coordinate frame name (capital script letters)
$a^{\mathscr{A}}$	-	variable expressed in the $\mathscr{A}$ coordinate frame
$\bar{a}$	-	column vector variable
a_x	-	the x-component of vector $\bar{a}$ (extends to y- and z-components)
$x_{\mathscr{A}}$	-	the x axis of the $\mathscr{A}$ coordinate frame (extends to y- and z-axes)
$\bar{r}_{\mathscr{A}/\mathscr{B}}$	-	r vector pointing to $\mathscr{A}$ with respect to $\mathscr{B}$
$[]^T$	-	superscript T indicates a transpose
A	-	matrix variable
A_{mxn}	-	matrix of m rows and n columns
I_{mxm}	-	identity matrix of m rows and m columns
$C_{\mathscr{A}_1}^{\mathscr{A}_2}$	-	3x3 Direction Cosine Matrix (DCM) which transforms a vector expressed in the $\mathscr{A}_1$ coordinate frame to the $\mathscr{A}_2$ coordinate frame when multiplied on the left of the vector
$s\phi$	-	$\sin(\phi)$
$c\phi$	-	$\cos(\phi)$
$s\theta$	-	$\sin(\theta)$
$c\theta$	-	$\cos(\theta)$
$s\psi$	-	$\sin(\psi)$
$c\psi$	-	$\cos(\psi)$

CHAPTER 1

INTRODUCTION

1.1 GPS-Denied and Image-Aided Navigation

Navigation, the process of accurately estimating states such as position and planning a course of travel, is an essential part of vehicle automation. Once these states are estimated, the vehicle can plan its course of travel and then apply control commands to get to where it needs to go. Without an accurate estimation of where the vehicle is, it could never accomplish its intended purpose.

The common backbone of most modern navigation systems consists of an inertial measurement unit (IMU) [1–3]. An IMU is composed of several accelerometers and gyroscopes. Much like the human ear, these sensors provide three-dimensional translation and rotation information to the vehicle in the form of accelerations and rotational rates. Given a starting location and orientation, these sensor readings enable the vehicle to estimate its orientation, or attitude, and position over time by integrating the sensor measurements. This integration process is called dead reckoning [4].

If the accelerometers and gyroscopes in an IMU were perfect, the vehicle could simply navigate by dead reckoning with no problems. However, there are always errors with these sensors such as misalignments, biases, and scaling factors because it is impossible to build a perfect sensor. These imperfections make navigation by dead reckoning over extended periods of time inaccurate and therefore unacceptable. The results would be similar to a human trying to walk from one end of their house to the other while closing their eyes and not feeling for obstacles.

To remedy this problem, more sensors may be added to the system to provide more information about the navigation states, such as position, velocity, and attitude. Unlike the IMU, these sensors, commonly referred to as aiding devices, provide useful information

through their measurements of the surrounding environment. These different measurements, if combined intelligently, can help the system by increasing state knowledge and minimizing uncertainty. It has become common practice to combine this information in what is called a Kalman filter. Kalman filters come in many varieties, but in the context of navigation, they are generally used to combine sensor information to provide state estimates and calculate a measure of certainty regarding the resulting estimates.

One of the most common and important aiding systems in modern vehicle automation and navigation is the global positioning system, or GPS [1–3]. However, GPS can be easily jammed and is often unreliable in environments such as natural and urban canyons [5, 6]. Situations or environments in which GPS is unreliable or denied are referred to as GPS-denied environments. Both military and civilian applications have fueled a growing interest in recent years to find effective GPS-denied navigation systems.

Image-aided navigation is one alternative to GPS-aided systems that has been explored extensively. Relevant works are discussed in the next section of this chapter. This method of navigation used to be impractical in real-time applications due to limitations of onboard sensors and processors in small vehicles. However, modern hardware has started to make image-aided navigation a real possibility and it has been proven to be a plausible mode of navigation when GPS is unavailable [1, 7]. Several ideas and algorithms related to making image-aided navigation work well have been developed in recent years [8–14].

Among the many versions of image-aided navigation, Wu et al. present a simple, yet promising algorithm that uses the line-of-sight (LOS) vectors from a monocular camera towards known landmarks to provide position and attitude information to the navigation system [7]. In this work, this type of measurement is referred to as a LOS measurement. The algorithm processes the image from the sensor, searching for landmarks with known positions in the environment. It then extracts useful information related to position and attitude for navigation from the observed angles of the LOS vector to the landmark by comparing its measurement to the estimated relative position of the landmark. Fig. 1.1 shows a representation of three LOS measurements being made to a lamp post, a mailbox,

and a traffic light in an urban environment. Similar measurements can be made to any landmark that is recognizable by image processing software.

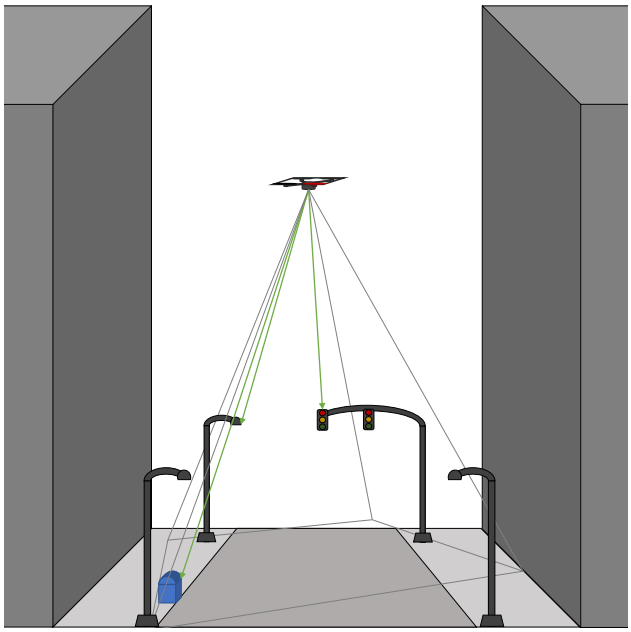

Fig. 1.1: A visual representation of navigation using line-of-sight measurements

Even though Wu et. al. proved the promise of these measurements in hardware during short simulated GPS outages, the impacts of many variables related to trajectory and landmark placement are not well understood [7]. There are several works which explore various landmark placement algorithms which will be discussed in the next chapter of this document. None, however, explore the relationships between vehicle trajectory, position uncertainty, relative position, and the distribution landmarks. This work explores these relationships by identifying and explaining various patterns observed by varying trajectory shape, altitude, and apparent landmark density. An equation describing the amount of information contained in a given measurement to a single landmark is presented along with some path-planning implications and applications.

1.2 Contributions

Image-aided navigation has recently become a hot topic and is no longer considered

new. As has been shown in the previous section, much work has been done exploring the uses of image-aided navigation. Contributions that the research in this work adds include the following:

1. A modular experimental framework was developed and implemented in MATLAB and SIMULINK which allows for easy manipulation of variables of interest. These variables include but are not limited to

    - a quadrotor model as developed by Beard that has been modified to use states expressed in the inertial frame and
    - a continuous-discrete Kalman filter that can incorporate GPS and/or LOS measurements for easy comparison.

2. A new derivation for the attitude portion of the measurement geometry matrix for LOS measurements for Euler angle attitude states rather than the quaternion version presented by Wu et. al. [7].

3. Image-aided navigation solutions were computed for over 540 unique combinations of trajectory shape, altitude, and landmark distribution. This data was then analyzed to identify patterns in the data which will be useful to areas such as path planning and landmark placement.

4. These resulting patterns were tied together in the derivation of the trace of the information matrix for LOS measurements. The resulting equation produces an estimate of how much information comes from a single measurement based on its relative position to the camera.

5. The analysis of the data uncovered several patterns which need to be explored further to better characterize LOS measurements, especially at lower altitudes. Any research areas uncovered by this analysis could be especially useful in path planning and landmark placement for small UAV applications in the future.

1.3 Overview

In order to explore the relationships mentioned above that will build upon previous work, several key elements are needed to provide realistic data for analysis. These elements are shown as the blocks in Fig. 1.2 as a step-by-step process along with any resulting data from each step. Steps 1-3 and the format of their resulting data is described in greater detail in chapter 2 of this work. To summarize these steps, a vehicle model with true-state feedback is first implemented and run to generate sensor data for several trajectories. The sensor data then has noise added to it and is combined in an extended Kalman filter (EKF) with dynamically created camera measurements (steps 2 and 3). This filter produces estimated states and a measure of estimate confidence called covariance. Results are organized and analyzed in steps 4 and 5, as detailed in chapters 3-4. Finally, conclusions are drawn and ideas for future work are discussed in chapter 6.

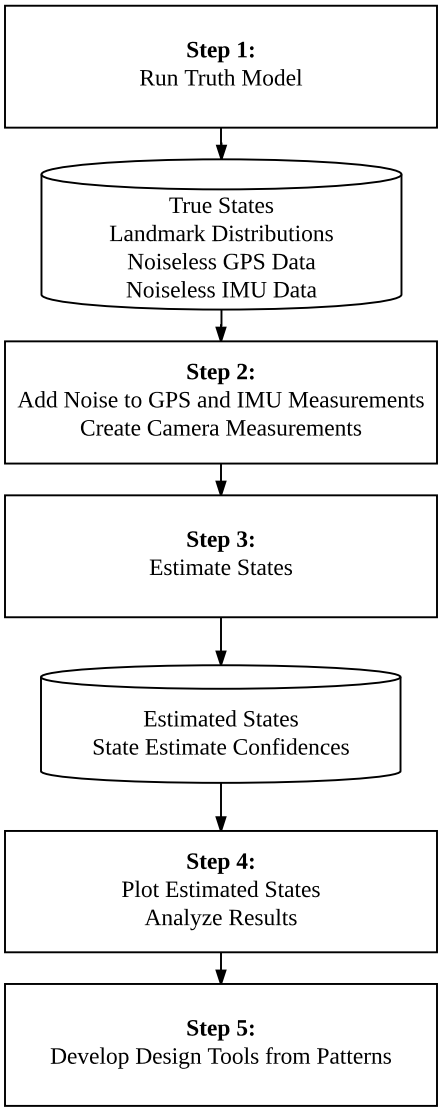

Fig. 1.2: Overview of experimentation process in block diagram form

CHAPTER 2

Background

As previously described, GPS-aided navigation systems have become commonplace in autonomous vehicles. Due to the publicly known frequency of GPS signals, both military and civilian users encounter problems with GPS signals [5, 6]. These problems continue to prompt an increased interest in alternative navigation aiding measurements. Various aiding sensors have been implemented, including imagers. Image-aided navigation is an attractive solution because most systems come equipped with a simple, small, and cost-effective system already installed. As was shown in several studies discussed below, image-aided navigation can be a promising solution for GPS-denied navigation problems.

One interesting form of image-aided navigation involved the placement of static sensors in the environment. Jourdan and Roy studied the placement of static sensors on the walls of buildings to minimize average position error [15]. Vitus and Tomlin later approached the problem with the intent of minimizing estimation error [16]. The problems with a static sensor method of aiding-measurements are twofold. First, it still relies on a continuous communication link between static sensors and the vehicle, making it less autonomous. Second, it is much more expensive to place multiple static sensors in the environment as the vehicle's travel area grows. Given these shortcomings, this work focuses on building upon knowledge of systems with on-board sensors.

In the world of unmanned aerial vehicles (UAVs), keeping the cost of the image sensor low is not difficult. This is partly because so many systems come already equipped with a simple imaging system consisting of a single-lens, or monocular, camera. The potential of these readily available systems has been noted by several navigation and guidance experts. A simple measurement model is set forth by Wu et. al., which shows how a pixel measurement can be compared to the estimated relative position of the landmark [7]. From this comparison, which is referred to as a line-of-sight, or LOS, measurement, they can find

position and attitude information. Though not a new form of measurement, they were able to show positive results in both simulation and in real-time hardware demonstrations.

This basic measurement has been built upon and extended in several ways, mostly in an effort to obtain depth information. Mohamed, Patra, and Lanzon added a few lasers to their system which were oriented to known angles [13]. Detecting the location of the laser dots in the image allows them to infer depth information. Sharma and Pack used the same basic measurement as Wu et. al. and then added a priori knowledge of the physical target size to get depth information [12]. Wang and Zhang et. al. independently decided to augment their LOS measurements with a preloaded depth map, allowing them to tap into a third dimensional measurement [9, 17]. Zhang et. al. later improved on their simulated data by applying their approach in hardware [18]. Bachrach et. al. took this approach one step further and attempted to also map the environment using a depth sensor with the camera.

This type of measurement is also useful in estimating target states. Sharma et. al. use bearing-only measurements in a cooperative setting to geo-localize a target [19]. The term bearing-only refers to the same type of measurement being discussed previously. Chowdary et. al. attempt to navigate without any a priori knowledge by using a version of simultaneous localization and mapping, or SLAM, that employs the same measurement model [11]. All of these references qualify the statement of interest in and use of the measurement presented by Wu as mentioned earlier.

Interest in this type of measurement has brought a wealth of questions forward that the authors address. Work by Sala et. al. briefly discusses what constitutes a good landmark and only chose landmarks that are always visible [10]. Several papers consider where to optimally place man-made landmarks, though most refer to a two-dimensional navigation problem [8, 20–22]. Most sources try to minimize the number of needed landmarks. Ahn et. al. try to do this by using a vanishing point method, but their method is limited to indoor flight [8]. One big question that is addressed extensively is that of path planning [14, 23, 24]. Bopardikar et. al. present an especially interesting approach to path planning in which

they realize both path distance and error covariance can be treated as costs. Path length is minimized first, while error covariance is treated second.

In all of this previous work, there has been no attempt to understand the relationship between vehicle trajectory, the number of visible landmarks, and the system's ability to maintain a high level of navigation confidence when using an LOS-type aiding measurement. There are several attempts in the works cited above to augment the system with extra sensors. However, it appears that our collective knowledge of system design is lacking when it comes to image-aided navigation because we do not fully understand the implications of this type of measurement. How much information does one LOS measurement give? What effect does trajectory altitude have on this kind of measurement? How much navigation confidence does the system gain for different apparent landmark densities at different altitudes? This work attempts to address these questions in an effort to provide a more informed approach to designing path-planning and guidance systems in the future.

CHAPTER 3

Methods

The previous chapter calls to attention a collective lack of knowledge regarding the relationship between trajectories, the number of measured ground landmarks, and the resulting navigation confidence. Fig. 1.2 then shows a method to generate data with the purpose of identifying patterns and eventually providing observations and tools that will aid in future guidance and path-planning algorithms. This chapter expands steps 1-3 of this method in detail.

Section 3.1 presents a description of the variables that were tested and why they were chosen. The experiment is then outlined in more detail including a description of each of the steps shown in Fig. 1.2. To facilitate the discussion of mathematics behind the system and data to be used, section 3.2 first identifies the coordinate frames used in this work. Next, the system's truth and sensor models from step 1 in Fig. 1.2 are described in detail in sections 3.3 and 3.4. The results are discussed later in section 4.

3.1 Experiment Overview

The purpose of this work is to provide valuable insight into the relationship between trajectories, the number of LOS-measurements to landmarks, and the resulting navigation confidence of LOS-type image-aided navigation. The overall approach of this experiment is to compare the EKF solution confidence of several scenarios that vary in trajectory shape, trajectory altitude, and landmark distributions. As will be described later in section 3.2.6, the camera is assumed to point in a nominally nadir direction.

3.1.1 Trajectory Shape

In this work, trajectory shape means the actual path and orientation that the vehicle travels. Nine different trajectory shapes were used to create sensor data for this experiment.

Three of these trajectories are loitering patterns that cause the vehicle to remain in a bounded area. The rest travel in different patterns along a line that is 100 meters long. Each trajectory is named and described in Table 3.1 below.

Table 3.1: List and description of trajectory shapes

Traj. Type	Traj. Name	Description
Loitering	Horizontal Circle	45 meter radius horizontal circle
	Horizontal Figure 8	60x60 meter horizontal figure 8
	Tilted Figure 8	60x60x20 meter tilted figure 8
Traveling	Line	100 meter straight line
Traveling	Twist Line	100 meter line, $\left[\frac{-\pi}{2}, \frac{\pi}{2}\right]$ varying heading
Traveling	Sine Line	100 meter horizontal sinusoid
Traveling	Alt. Sine Line	100 meter vertical sinusoid
Traveling	Tilted Sine Line	100 meter horizontal and vertical sinusoid
Traveling	Corkscrew	100 meter corkscrew

3.1.2 Altitude

Altitude is defined in this work as the relative distance from the ground to the vehicle's center of mass as measured along the negative z-axis of the inertial frame (see section 3.2.1 for a description of the inertial frame). Altitudes within all trajectory shapes included in this work are kept relatively constant to facilitate the comparison of landmark measurements at each altitude. At the beginning of this work, it was unknown what range in altitude would be the most informative and interesting to examine. The six linearly separated altitudes in Table 3.2 are considered in this survey. This sampling of altitudes was chosen to create data points that spread across a wide range of applications, therefore making the results more generally valuable.

Table 3.2: List of trajectory altitudes

Altitude [meters]
15
412
809
1206
1603
2000

3.1.3 Apparent Landmark Densities

There are two challenges with this experiment when dealing with landmark distributions because this work seeks to compare changes in two variables that are correlated: altitude and the number of observed landmarks in a given image. First, when comparing altitude results it is important to measure the same number of landmarks at each altitude. At the same time, it is equally important to maintain a similar perceived landmark spacing at each altitude. This is done by creating one landmark distribution for each altitude where the angular distance to the camera is maintained for each altitude. One set of landmark distributions that meets these criteria across all the altitudes is called an apparent landmark density, or ALD, for the remainder of this work. Using different landmark distributions with the same apparent density tricks the vehicle into making similar LOS measurements at different altitudes. An example of this is given in Fig. 3.1. Both plots show the same corkscrew trajectory shape in red, but at two different altitudes (15 and 412 meters). The blue circles represent the landmarks on the ground. On the left, the landmarks are physically much closer together than those on the right. However, because of the difference in vehicle altitude, they appear to the camera to have the same density. For this example, the vehicle expects to see at most four landmarks at a time, even though the landmarks are physically spaced differently in the two scenes.

The second challenge is in being able to compare the number of observed landmarks. This is made possible by creating several distribution sets with different apparent landmark densities. This work examines the effect of 10 ALDs at each altitude. For future clarity,

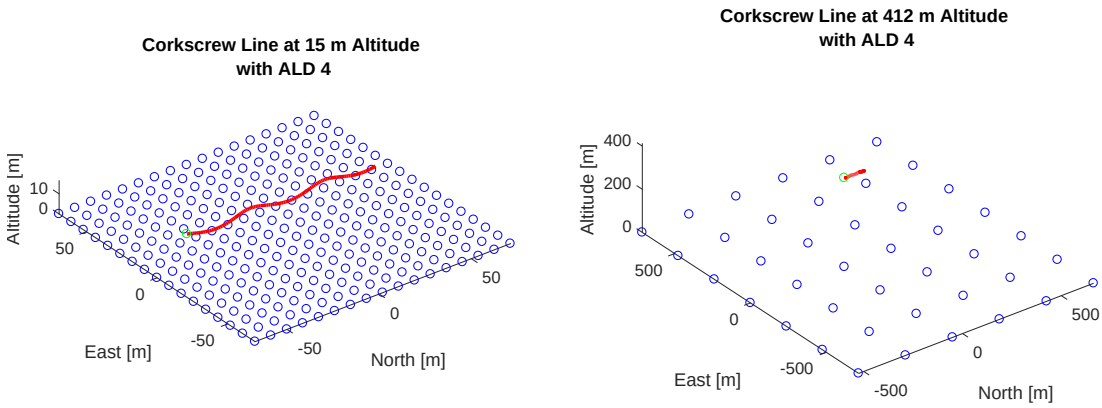

Fig. 3.1: Example of maintaining an ALD across altitudes

ALDs are named in this work with a number 1 to 10. These ALD numbers refer to the maximum number of landmarks the camera should be able to observe within its 30×20 degree field of view on the ground when flying flat and level.

Landmarks in each scene are distributed into uniform grids to avoid making measurements with too much redundant navigation information. Though not usually realistic, doing this maximizes the amount of measurement geometry information available in each image from the camera.

3.1.4 Experiment Outline

To observe and explain the patterns and relationships between these variables, each of the steps from Fig. 1.2 are completed. Step 1 independently runs each combination of trajectory shape and altitude. Each landmark distribution is created also as part of step 1. The resulting data included noiseless vehicle position, velocity, and attitude states; noiseless GPS measurements at 1 Hz; noiseless accelerometer and gyroscope data at 200 Hz; and 10 ALDs made up of 10 landmark distributions for each of the six altitudes.

Steps 2 and 3 must be taken together for each combination of trajectory shape, altitude, and ALD. For a given combination, the previously generated sensor data first has random white noise injected into it. The camera measurements are also created and have random noise injected into them as well. When all of these measurements are prepared, they are

run through an extended Kalman filter (EKF) in step 3. The EKF produces a set of estimated states for that trajectory, altitude, and ALD combination along with a measure of its confidence called covariance. This data is stored to be compared and analyzed later. Steps 2 and 3 are run again for each combination, applying new random noise to each sensor measurement at each iteration.

Next, the EKF results are plotted in step 4 and examined to identify interesting patterns. Step 5 is finally applied when these patterns are used to develop relationships that can be used in design tools in future work. These last two steps are treated in chapter 4.

3.2 Coordinate Frames

It is often useful to express different subsystems and variables relative to each other from different perspectives. Doing so can modularize the way the system is viewed and can serve to simplify the math that describes and relates these subsystems. Coordinate frames simply define the views from which states can be observed. This section describes the relationships between each of the coordinate frames used in this work. The relationships between the $\mathscr{I}$-frame, $\mathscr{V}$-frame, $\mathscr{V}_1$-frame, $\mathscr{V}_2$-frame, and $\mathscr{B}$-frame are all patterned after work by Beard and McLain [3]. All rotations described below and throughout the remainder of this work follow the conventions of the right-hand rule. Also, for clarity in the figures contained in this section, the red portions of the quadrotor drawings indicate the "front" of the vehicle.

3.2.1 Inertial $\mathscr{I}$-Frame

The inertial, or $\mathscr{I}$-frame, is a static coordinate frame whose x, y, and z-axes point north, east, and down (towards earth center), respectively. This type of static orientation is referred to as north-east-down, or NED, for the remainder of this work. The origin of the $\mathscr{I}$-frame is defined to be the reference origin. In this work, all vehicle and landmark position values are measured with reference to this origin location. Fig. 3.2 in the following subsection gives a visual representation of the $\mathscr{I}$-frame. It is important at this point to acknowledge that the $\mathscr{I}$-frame is fixed to the earth and therefore the rotation of the earth

is ignored for simplicity.

3.2.2 Vehicle $\mathscr{V}$-Frame

The $\mathscr{V}$-frame is constantly aligned with the $\mathscr{I}$-frame, meaning that it is an NED frame as described in section 3.2.1. Its origin, however, is always collocated with the center of mass of the vehicle as shown in Fig. 3.2.

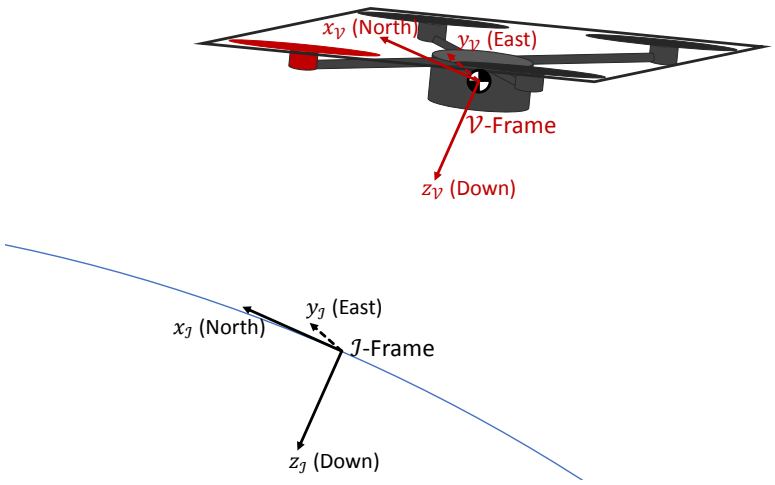

Fig. 3.2: Relationship between the inertial and vehicle frames

The transformation of a vector from the $\mathscr{I}$-frame to the $\mathscr{V}$-frame is given by

$$\bar{a}^{\mathscr{V}} = C_{\mathscr{I}}^{\mathscr{V}} \bar{a}^{\mathscr{I}} \tag{3.1}$$

where

$$C_{\mathscr{I}}^{\mathscr{V}} = I_{3x3}. \tag{3.2}$$

3.2.3 Vehicle-1 $\mathscr{V}1$-Frame

The origin of the $\mathscr{V}_1$-frame is collocated with the origin of the $\mathscr{V}$-frame. Its orientation is obtained by rotating the $\mathscr{V}$-frame about its z-axis by the vehicle's yaw angle, ψ. This results in the $\mathscr{V}_1$-frame's z-axis pointing down towards earth center. If the vehicle had no

pitch or roll, the x-axis would point directly out the front of the vehicle and the y-axis would point directly out the starboard side of the vehicle. This relationship is shown in Fig. 3.3.

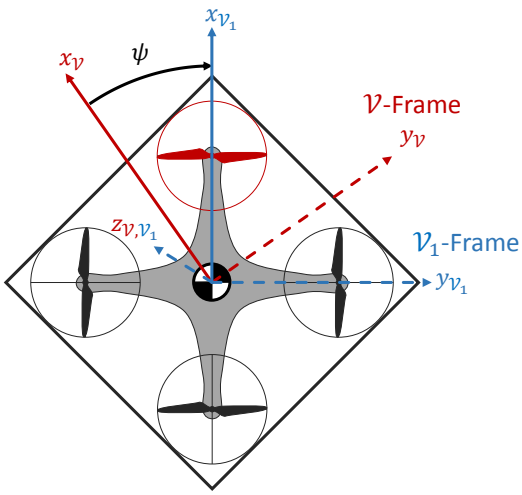

Fig. 3.3: Relationship between the vehicle and vehicle-1 frames

The transformation of a vector from the $\mathscr{V}$-frame to the $\mathscr{V}_1$-frame is given by

$$\bar{a}^{\mathscr{V}_1} = C_{\mathscr{V}}^{\mathscr{V}_1} \bar{a}^{\mathscr{V}} \tag{3.3}$$

where

$$C_{\mathscr{V}}^{\mathscr{V}_1} = \begin{bmatrix} \cos\psi & \sin\psi & 0 \\ -\sin\psi & \cos\psi & 0 \\ 0 & 0 & 1 \end{bmatrix}. \tag{3.4}$$

3.2.4 Vehicle-2 $\mathscr{V}2$-Frame

The origin of the $\mathscr{V}_2$-frame is collocated with the origin of the $\mathscr{V}$- and $\mathscr{V}_1$-frames. However, its orientation is obtained by rotating the $\mathscr{V}_1$-frame about its y-axis by the vehicle's pitch angle, θ. This results in the $\mathscr{V}_2$-frame's z-axis pointing straight down out of the vehicle and the x-axis pointing directly out the front of the vehicle. If the vehicle had no roll, the y-axis would point directly out the starboard side of the vehicle as shown in Fig. 3.4.

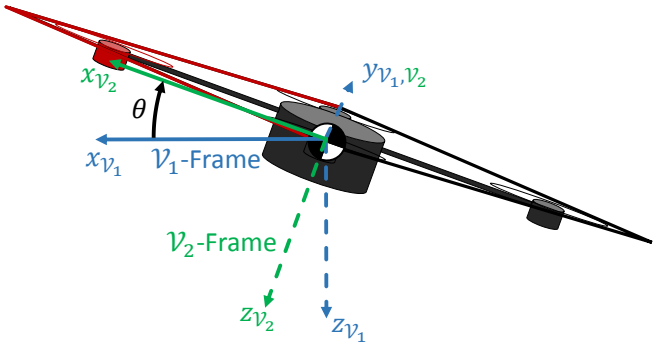

Fig. 3.4: Relationship between the vehicle-1 and vehicle-2 frames

This transformation of a vector from the $\mathscr{V}_1$-frame to the $\mathscr{V}_2$-frame is given by

$$\bar{a}^{\mathscr{V}_2} = C_{\mathscr{V}_1}^{\mathscr{V}_2} \bar{a}^{\mathscr{V}_1} \tag{3.5}$$

where

$$C_{\mathscr{V}_1}^{\mathscr{V}_2} = \begin{bmatrix} \cos\theta & 0 & -\sin\theta \\ 0 & 1 & 0 \\ \sin\theta & 0 & \cos\theta \end{bmatrix}. \tag{3.6}$$

3.2.5 Body $\mathscr{B}$-Frame

The body, or $\mathscr{B}$-frame, is collocated with the center of mass of the vehicle, just as the $\mathscr{V}$, $\mathscr{V}_1$, and $\mathscr{V}_2$ frames are. The orientation of the $\mathscr{B}$-frame is obtained by rotating the $\mathscr{V}_2$-frame about its x-axis by the vehicle roll angle, ϕ. This results in the $\mathscr{B}$-frame's x-axis always pointing out the front of the vehicle, the y-axis always pointing out the right of the vehicle, and the z-axis always pointing out the bottom of the vehicle as shown in Fig. 3.5.

The transformation of a vector from the $\mathscr{V}_2$-frame to the $\mathscr{B}$-frame is given by

$$\bar{a}^{\mathscr{B}} = C_{\mathscr{V}_2}^{\mathscr{B}} \bar{a}^{\mathscr{V}_2} \tag{3.7}$$

where

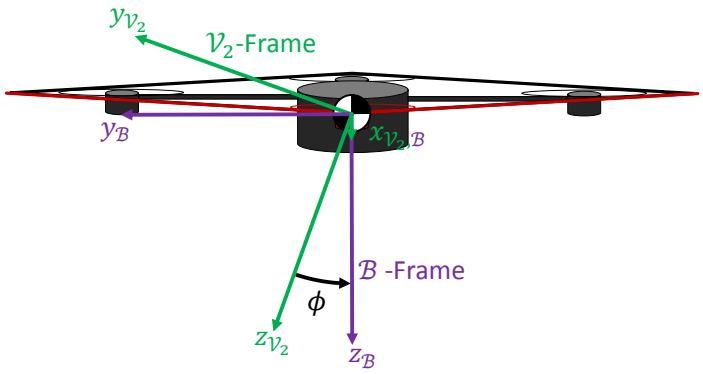

Fig. 3.5: Relationship between the vehicle-2 and body frames

$$C_{\mathscr{V}_2}^{\mathscr{B}} = \begin{bmatrix} 1 & 0 & 0 \\ 0 & \cos\phi & \sin\phi \\ 0 & -\sin\phi & \cos\phi \end{bmatrix}. \tag{3.8}$$

At this point, it is appropriate to show that a complete transformation of a vector from the $\mathscr{V}$-frame to the $\mathscr{B}$-frame may be mathematically obtained by

$$\bar{a}^{\mathscr{B}} = C_{\mathscr{V}_2}^{\mathscr{B}} C_{\mathscr{V}_1}^{\mathscr{V}_2} C_{\mathscr{V}}^{\mathscr{V}_1} \bar{a}^{\mathscr{V}} \tag{3.9}$$

$$= C_{\mathscr{V}}^{\mathscr{B}} \bar{a}^{\mathscr{V}} \tag{3.10}$$

where ϕ, θ, and ψ are roll, pitch, and yaw Euler angles, respectively,

$$C_{\mathscr{V}}^{\mathscr{B}} = \begin{bmatrix} c\theta c\psi & c\theta s\psi & -s\theta \\ s\phi s\theta c\psi - c\phi s\psi & s\phi s\theta s\psi + c\phi c\psi & s\phi c\theta \\ c\phi s\theta c\psi + s\phi s\psi & c\phi s\theta s\psi - s\phi c\psi & c\phi c\theta \end{bmatrix}, \tag{3.11}$$

and

$$c\phi = \cos\phi \tag{3.12}$$

$$c\theta = \cos\theta \tag{3.13}$$

$$c\psi = \cos\psi \tag{3.14}$$

$$s\phi = \sin\phi \tag{3.15}$$

$$s\theta = \sin\theta \tag{3.16}$$

$$s\psi = \sin\psi. \tag{3.17}$$

For later derivations in this work, the following values of $C_{\mathscr{V}}^{\mathscr{B}}$ are defined for convenience and space

$$\begin{bmatrix} c_{11} & c_{12} & c_{13} \\ c_{21} & c_{22} & c_{23} \\ c_{31} & c_{32} & c_{33} \end{bmatrix} = \begin{bmatrix} c\theta c\psi & c\theta s\psi & -s\theta \\ s\phi s\theta c\psi - c\phi s\psi & s\phi s\theta s\psi + c\phi c\psi & s\phi c\theta \\ c\phi s\theta c\psi + s\phi s\psi & c\phi s\theta s\psi - s\phi c\psi & c\phi c\theta \end{bmatrix}. \tag{3.18}$$

3.2.6 Camera $\mathscr{F}$-Frame

In dealing with a camera, a new frame needs to be introduced to account for the orientation of the camera with respect to the vehicle. This makes it possible to relate camera measurements to the vehicle orientation and position. This new camera frame, or $\mathscr{F}$-frame, is collocated at the center of mass to simplify the math in later derivations. Since the camera model is not gimbaled, its orientation is obtained by rotating the $\mathscr{B}$-frame by -90 degrees or $\frac{\pi}{2}$ radians about its y-axis. This results in the $\mathscr{F}$-frame's x-axis pointing down out the bottom of the vehicle's body along the $\mathscr{B}$-frame's z-axis. The assumption here is that the focal point of the camera is also located at the center of mass of the vehicle. See Fig. 3.6 for a visual representation of the $\mathscr{F}$-frame with respect to the $\mathscr{B}$-frame.

The transformation of a vector from the $\mathscr{B}$-frame to the $\mathscr{F}$-frame is given by

$$\bar{a}^{\mathscr{F}} = C_{\mathscr{B}}^{\mathscr{F}} \bar{a}^{\mathscr{B}} \tag{3.19}$$

where

$$C_{\mathscr{B}}^{\mathscr{F}} = \begin{bmatrix} \cos\left(-\frac{\pi}{2}\right) & 0 & -\sin\left(-\frac{\pi}{2}\right) \\ 0 & 1 & 0 \\ \sin\left(-\frac{\pi}{2}\right) & 0 & \cos\left(-\frac{\pi}{2}\right) \end{bmatrix} \tag{3.20}$$

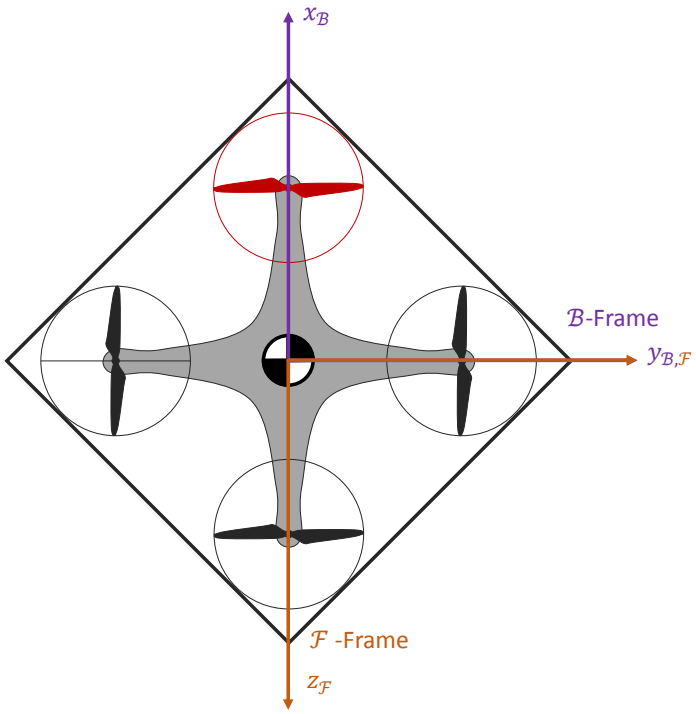

Fig. 3.6: Relationship between the body and camera frames

$$= \begin{bmatrix} 0 & 0 & 1 \\ 0 & 1 & 0 \\ -1 & 0 & 0 \end{bmatrix}. \tag{3.21}$$

3.2.7 Image $\mathscr{X}$-Frame

Since camera measurements are obtained as pixel locations, it is necessary for a frame to be defined describing the orientation of the image focal plane. Image pixels are typically referred to as having the positive x-direction increasing to the right along a row of pixels, while the positive y-direction increases down the image along the column of pixels [25]. For this work, the camera is oriented such that the top of the image is nearest the front of the vehicle with the x-axis of the $\mathscr{X}$-frame pointing out the right of the vehicle. The origin of the $\mathscr{X}$-frame is located at a distance of the camera's focal length along the $\mathscr{F}$-frame's x-axis and shifted over from the center of the image to the top-left of the image plane (distances given by the camera's principle point in pixels). The $\mathscr{X}$-frame's y-axis points out the back

of the vehicle and its z-axis points down out the bottom of the vehicle. This is visually represented in Fig. 3.7.

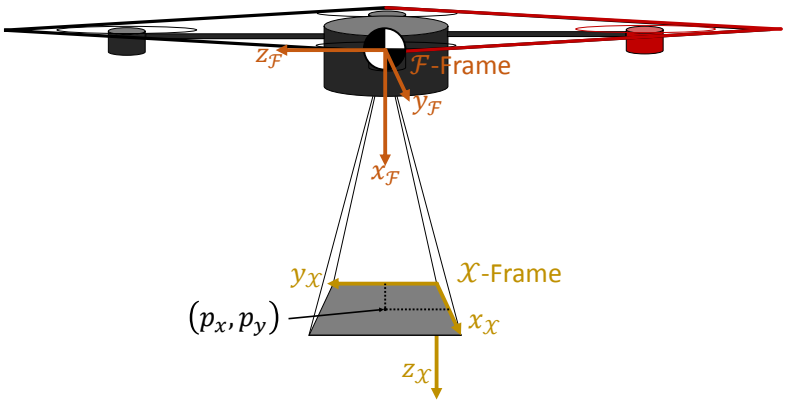

Fig. 3.7: Relationship between the body and camera frames

The transformation of a vector from the $\mathscr{F}$-frame to the $\mathscr{X}$-frame is given by

$$\bar{a}^{\mathscr{X}} = C_{\mathscr{F}}^{\mathscr{X}} \bar{a}^{\mathscr{F}} \tag{3.22}$$

where

$$C_{\mathscr{F}}^{\mathscr{X}} = \begin{bmatrix} 0 & 1 & 0 \\ 0 & 0 & 1 \\ 1 & 0 & 0 \end{bmatrix}. \tag{3.23}$$

3.3 System Truth Model

With a firm understanding of its coordinate frames, this section now describes the system truth model to be used in step 1 shown in Fig. 1.2. The vehicle system used in this work is a small quadrotor unmanned aerial vehicle. As mentioned in section 3.1, this model was run several times to produce noiseless sensor data for each trajectory shape and altitude.

Conceptually, this system is organized much like a classical control system where the

feedback is a pure feedback. This means that the control system operates off of true states. Though this is not realistic in a hardware system, this is appropriate for this simulation as it still provides simulation data that is representative of quadrotor kinematics and dynamics. To better understand the components of this system, Fig. 3.8 shows step 1 of Fig. 1.2 expanded to its own functional block diagram. Each block can be treated as a mathematical function with inputs and outputs. Each block's inputs, outputs, and underlying mathematics are described in the following subsections.

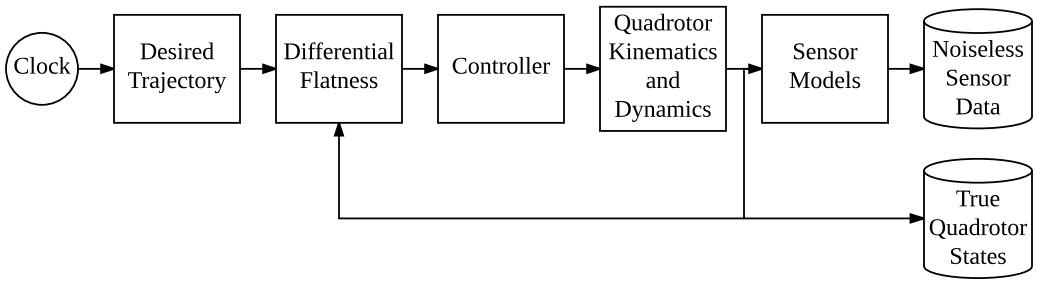

Fig. 3.8: Overview of truth model process in block diagram form

Note that the sensor models and their resulting measurements are treated in section 3.4.

3.3.1 System States

Quantities described in this work are expressed in terms of the vehicle state vector components. The quadrotor state vector, $\bar{x}$ consists of the following 12 states:

$p_n^{\mathscr{I}}$ - the inertial north position of the quadrotor along the x-axis of the $\mathscr{I}$-frame

$p_e^{\mathscr{I}}$ - the inertial east position of the quadrotor along the y-axis of the $\mathscr{I}$-frame

$p_d^{\mathscr{I}}$ - the inertial down position of the quadrotor along the z-axis of the $\mathscr{I}$-frame

$v_n^{\mathscr{I}}$ - the inertial north velocity of the quadrotor along the x-axis of the $\mathscr{I}$-frame

$v_e^{\mathscr{I}}$ - the inertial east velocity of the quadrotor along the y-axis of the $\mathscr{I}$-frame

$v_d^{\mathscr{I}}$ - the inertial down velocity of the quadrotor along the z-axis of the $\mathscr{I}$-frame

ϕ - the roll angle defined as the positive right-hand rotation about the x-axis of the $\mathscr{V}_2$-frame

θ - the pitch angle defined as the positive right-hand rotation about the y-axis of the $\mathscr{V}_1$-frame

ψ - the yaw angle defined as the positive right-hand rotation about the z-axis of the $\mathscr{V}$-frame

p - the roll rate measured about the x-axis of the $\mathscr{B}$-frame

q - the pitch rate measured about the y-axis of the $\mathscr{B}$-frame

r - the yaw rate measured about the z-axis of the $\mathscr{B}$-frame

These states are modeled after work done by Beard, though position and velocity states are given in the inertial frame as opposed to having the velocity states in the body frame [26]. Three-dimensional position, velocity, and attitude are referred as $\bar{p}$, $\bar{v}$, and $\bar{\alpha}$ column vectors for the remainder of this work.

3.3.2 System Kinematics and Dynamics Model

The derivation of the system kinematics and dynamics is also based on Beard's same work [26]. He solves for the following constant inertia matrix J which assumes that the vehicle is inertially symmetric about each of its axes:

$$J = \begin{bmatrix} J_x & 0 & 0 \\ 0 & J_y & 0 \\ 0 & 0 & J_z \end{bmatrix}. \tag{3.24}$$

The inverse of this inertia matrix can be expressed for later use as

$$J^{-1} = \begin{bmatrix} \frac{1}{J_x} & 0 & 0 \\ 0 & \frac{1}{J_y} & 0 \\ 0 & 0 & \frac{1}{J_z} \end{bmatrix}. \tag{3.25}$$

The four propellers on the quadrotor work together to produce both torque and lift. The three-dimensional torques produced by the motors expressed in the $\mathscr{B}$-frame are defined as

$$\bar{\tau}^{\mathscr{B}} = \begin{bmatrix} \tau_\phi \\ \tau_\theta \\ \tau_\psi \end{bmatrix}. \tag{3.26}$$

Expressions for $\bar{a}_g^{\mathscr{I}}$ as the acceleration due to gravity expressed in the $\mathscr{I}$-frame, g as the value of gravitational acceleration, and $\bar{a}_{thrust}^{\mathscr{B}}$ as the acceleration due to the thrust expressed in the $\mathscr{B}$-frame are defined as

$$\bar{a}_g^{\mathscr{I}} = \begin{bmatrix} 0 \\ 0 \\ g \end{bmatrix} \tag{3.27}$$

$$g \approx 9.81 \frac{\mathrm{m}}{\mathrm{s}} \tag{3.28}$$

$$\bar{a}^{\mathscr{B}}_{thrust} = \begin{bmatrix} 0 \\ 0 \\ -\frac{F_T}{m} \end{bmatrix} \tag{3.29}$$

where F_T is the force of the thrust along the z-axis of the $\mathscr{B}$-frame, and m is the mass of the vehicle.

Using these definitions, the six degree of freedom model for the quadrotor's kinematics and dynamics can be summarized as

$$\dot{\bar{x}} = \begin{bmatrix} \dot{\bar{p}}^{\mathscr{I}} \\ \dot{\bar{v}}^{\mathscr{I}} \\ \dot{\bar{\alpha}} \\ \dot{\bar{\omega}} \end{bmatrix} = \begin{bmatrix} \dot{\bar{v}}^{\mathscr{I}} \\ \bar{a}^{\mathscr{I}}_g + C^{\mathscr{I}}_{\mathscr{B}} \bar{a}^{\mathscr{B}}_{thrust} \\ \begin{bmatrix} \frac{J_y - J_z}{J_x} qr \\ \frac{J_z - J_x}{J_y} pr \\ \frac{J_x - J_y}{J_z} pq \end{bmatrix} + J^{-1} \bar{\tau}^{\mathscr{B}} \\ J^{-1} \bar{\tau}^{\mathscr{B}} \end{bmatrix}. \tag{3.30}$$

3.3.3 Controls and Desired Trajectories

Rather than inventing or re-deriving a novel method of controls, this work follows the work done by Ferrin et. al. on controls using differential flatness [27]. They make the matter of controlling the vehicle a relatively simple and straight forward process. The reader is directed to their paper for a full explanation of differential flatness and their ensuing algorithm, as only a brief summary is presented here.

The differential flatness algorithm accepts the desired trajectory's differentially flat position and heading with their first and second time derivatives. It uses these values to calculate the state and reference inputs. The current vehicle states are subtracted from the desired states, passed through a linear quadratic regulator (LQR) controller and finally re-combined with the reference inputs. These quantities are run through a simple proportional, integral, derivative (PID) controller to control the attitude and thrust.

3.3.4 Desired Trajectories

The desired trajectories have already been named at the beginning of section 3.1. However, it is important to mention what general elements make up each of the trajectories. Each trajectory was simply a function of time and had the following outputs:

$\bar{p}^{\mathcal{I}}_{desired}$	-	desired position
$\dot{\bar{p}}^{\mathcal{I}}_{desired}$	-	desired velocity, or time derivative of $\bar{p}^{\mathcal{I}}_{desired}$
$\ddot{\bar{p}}^{\mathcal{I}}_{desired}$	-	desired acceleration, or double time derivative of $\bar{p}^{\mathcal{I}}_{desired}$
$\psi_{desired}$	-	desired heading
$\dot{\psi}_{desired}$	-	desired heading rate, or time derivative of $\theta_{desired}$
$\ddot{\psi}_{desired}$	-	desired heading angular acceleration, or double time derivative of $\theta_{desired}$

3.4 Sensor Models

As discussed in the introduction, a navigation system is typically built with several sensors to aid in state estimation. Generally, the basic building blocks in navigation systems include accelerometers, gyroscopes, and GPS. Measurements from these sensors are then often combined in some form of Kalman filter to estimate system states such as position, velocity, and attitude. These sensors were modeled and implemented in Simulink to output perfect, noiseless measurements. However, as shown in Fig. 3.8, these sensor values were not included in the model's feedback control.

The following subsections describe each sensor model along with any assumptions. A model for GPS measurements is included because GPS-aided solutions are created for each trajectory shape and altitude. These results are used later as a performance baseline to which image-aided solutions are compared. A camera model is also included and discussed in detail to provide LOS measurements.

3.4.1 Accelerometers

Accelerometers measure the rate of change of the velocity in the $\mathscr{B}$-frame. True acceleration due to system forces (no external forces such as wind) can be expressed for this system as

$$\bar{a}^{\mathscr{B}} = \begin{bmatrix} 0 \\ 0 \\ -\frac{f_T}{m} \end{bmatrix} \tag{3.31}$$

where f_T is the force due to the trust generated by the actuators and m is the mass of the vehicle. Gravity is an environmentally induced acceleration and cannot be detected directly by the accelerometers. It is introduced into the measurements via the system dynamics equations detailed earlier. To simplify the model, wind conditions are assumed to be zero since they should not have any affect on navigation solution confidence.

Real accelerometers are often modeled to include various error sources. These error sources may include biases, scale factors, internal misalignments, and mounting misalignments. It is common practice in many applications to use the navigation system's Kalman filter to settle on a more accurate estimation of these error sources. Since this work does not explore the efficacy of LOS measurements in estimating those error sources, this work assumes a good estimation of them has already been obtained and applied. Though it is impossible to perfectly determine the exact values of these error sources in real life, it is sufficient for this application to model the error sources as Gaussian, random white noise. Thus, the sensor model becomes

$$\tilde{\bar{a}}^{\mathscr{B}} = \begin{bmatrix} 0 \\ 0 \\ -\frac{f_T}{m} \end{bmatrix} + \eta_{accel} \tag{3.32}$$

where η_{accel} is zero mean white noise of strength σ_{accel}. New random white noise errors are only added each time the measurements are fed into the state estimation filter.

3.4.2 Gyroscopes

Gyroscopes measure angular rate. Angular rates induced by the system are modeled as

$$\bar{\omega} = \begin{bmatrix} p \\ q \\ r \end{bmatrix} \tag{3.33}$$

where p, q, and r are defined as the the roll, pitch, and yaw rates measured about the axes of the $\mathscr{B}$-frame as defined in section 3.3.1.

Real gyroscopes suffer from the same types of error sources as accelerometers. Following the same logic as in section 3.4.1, these error sources can be simplified for this application to simple Gaussian, random white noise. Therefore, the sensor model becomes

$$\tilde{\bar{\omega}} = \begin{bmatrix} p \\ q \\ r \end{bmatrix} + \eta_{gryo} \tag{3.34}$$

where η_{gryo} is zero mean white noise of strength σ_{gryo}. New random white noise errors are only added each time the measurements are fed into the state estimation filter.

3.4.3 GPS

Global positioning system, or GPS, uses pseudo-range measurements to calculate a measure of three-dimensional position. Carrier phase Doppler measurements from GPS can also be used to calculate three-dimensional velocity [3]. It is assumed that the GPS used in this system provides north, east, and up measurements of both position and velocity with respect to the inertial reference $\mathscr{I}$-frame rather than in latitude, longitude, and altitude:

$$\tilde{\bar{p}}^{\mathscr{I}} = \begin{bmatrix} \tilde{p}_n^{\mathscr{I}} \\ \tilde{p}_e^{\mathscr{I}} \\ \tilde{p}_h^{\mathscr{I}} \end{bmatrix} \tag{3.35}$$

$$\tilde{\bar{v}}^{\mathscr{I}} = \begin{bmatrix} \tilde{v}_n^{\mathscr{I}} \\ \tilde{v}_e^{\mathscr{I}} \\ \tilde{v}_h^{\mathscr{I}} \end{bmatrix}. \tag{3.36}$$

Note that $\tilde{p}_h^{\mathscr{I}}$ is the height or altitude position with respect to the $\mathscr{I}$-frame, measured positively along the negative z-axis of the $\mathscr{I}$-frame. It follows that $\tilde{v}_h^{\mathscr{I}}$ is the velocity of the vehicle along the negative z-axis of the $\mathscr{I}$-frame.

These were combined to a single measurement vector, $\tilde{\bar{\gamma}}_{GPS}$:

$$\tilde{\bar{\gamma}}_{GPS} = \begin{bmatrix} \tilde{p}_n^{\mathscr{I}} \\ \tilde{p}_e^{\mathscr{I}} \\ \tilde{p}_h^{\mathscr{I}} \\ \tilde{v}_n^{\mathscr{I}} \\ \tilde{v}_e^{\mathscr{I}} \\ \tilde{v}_h^{\mathscr{I}} \end{bmatrix}. \tag{3.37}$$

GPS measurement noise should be modeled as a Gauss-Markov process. However, since this work does not include bias estimations, the GPS measurement noise is modeled as Gaussian white noise like in the cases of IMU sensors discussed earlier. GPS measurements with noise added thus become

$$\tilde{\bar{\gamma}}_{\gamma} = \begin{bmatrix} \tilde{p}_n^{\mathscr{I}} \\ \tilde{p}_e^{\mathscr{I}} \\ \tilde{p}_h^{\mathscr{I}} \\ \tilde{v}_n^{\mathscr{I}} \\ \tilde{v}_e^{\mathscr{I}} \\ \tilde{v}_h^{\mathscr{I}} \end{bmatrix} + \eta_{\gamma} \tag{3.38}$$

where η_{γ} is zero mean white noise. The terms corresponding to position measurements are of strength σ_{γ_p} and terms corresponding to velocity measurements are of strength σ_{γ_v}. New random white noise errors are only added each time the measurements are fed into the state

estimation filter.

3.4.4 Camera

Much like the work described by Wu et. al., the camera sensor model is divided into two parts. First, they defined a perspective projection model of a basic, ideal pinhole camera [7]. This model projects the three-dimensional landmark location onto the two-dimensional image plane. This projection is shown in Fig. 3.9. It is worth noting here that the camera model used in this work has a 30×20 degree field of view.

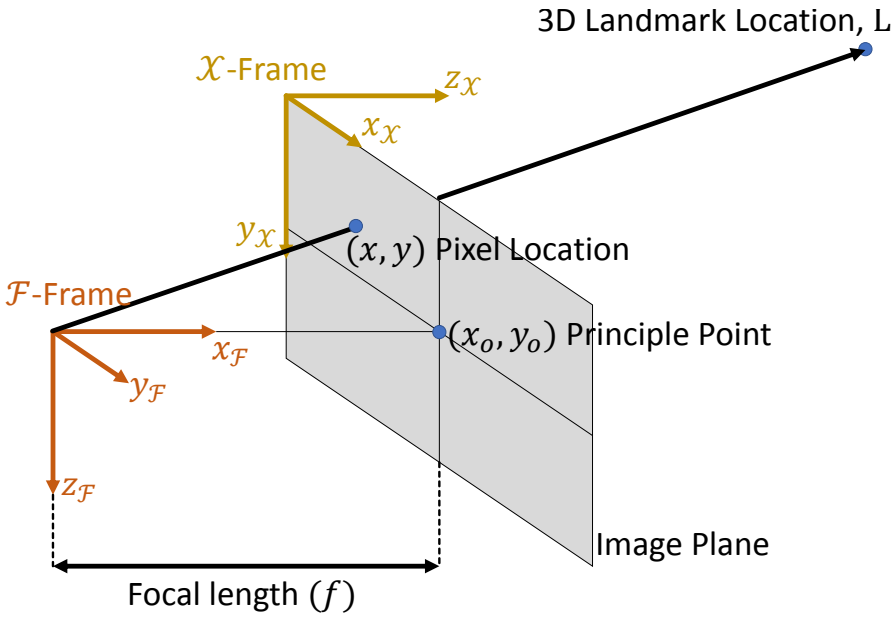

Fig. 3.9: Representation of pinhole camera perspective projection

The undistorted, two-dimensional pixel position in the image plane, (x_u, y_u), is given by the following equations:

$$x_u = x_o - f_x \frac{r^{\mathscr{X}}_{L/\mathscr{F},x}}{r^{\mathscr{X}}_{L/\mathscr{F},z}} \tag{3.39}$$

$$y_u = y_o - f_y \frac{r^{\mathscr{X}}_{L/\mathscr{F},y}}{r^{\mathscr{X}}_{L/\mathscr{F},z}} \tag{3.40}$$

where f_x and f_y are the camera's horizontal and vertical focal lengths, respectively, (x_o, y_o)

is the camera's principle point, and $\bar{r}^{\mathscr{X}}_{L/\mathscr{F}}$ is the position vector of the landmark with respect to the focal point of the camera expressed in the $\mathscr{X}$-frame. In simulation, the camera is assumed to have identical horizontal and vertical focal lengths. Thus, $f = f_x = f_y$.

Realistically, a simple pinhole camera model is not an adequate representation of the problem. With a real camera, the image would be distorted by the lens and therefore would need to be undistorted. Because the effects of the camera are so central to this work, this distortion is also implemented and then the equations to remove the distortion are applied. The process of distorting the image in simulation to mimic the effects of a real-world camera is a more complicated, iterative process. Due to the space required to discuss this process, the reader is referred to Brown's work [25]. The distorted pixel locations are referred to here as $(x_{d,noiseless}, y_{d,noiseless})$.

LOS measurement noise must be added to the distorted pixel measurement, since that is where the noise occurs in a real camera. Noise in this sensor, $\eta_{\delta\lambda}$, is a Gaussian white noise of strength $\sigma_{\delta\lambda}$. However, it is defined as an angular measurement noise and therefore must be added in angle space rather than in pixel space by using the equations:

$$x_d = x_{d,noiseless} + f_x \eta_{\delta\lambda,x} \tag{3.41}$$

$$y_d = y_{d,noiseless} + f_y \eta_{\delta\lambda,y}. \tag{3.42}$$

After noise has been added to the distorted pixel location, the measurement is ready to be undistorted. Brown does define a common, simple set of equations for removing the distortion and revealing the undistorted location of the landmark on the image plane. These equations are altered slightly for this application to give:

$$x_u = x_d \left(1 + k_1 r^2 + k_2 r^4\right) 2p_1 x_d y_d + p_2 \left(r^2 + 2x_d^2\right) \tag{3.43}$$

$$y_u = y_d \left(1 + k_1 r^2 + k_2 r^4\right) 2p_2 x_d y_d + p_1 \left(r^2 + 2y_d^2\right) \tag{3.44}$$

where x_d and y_d are the distorted pixel locations as they would be given in the $\mathscr{X}$-frame by the physical camera and r is the distance from the camera's principle point. The rest of

the variables are the following camera parameters:

$$(p_1, p_2) = \text{principle point} \tag{3.45}$$

$$(k_1, k2) = \text{radial distortion coefficient with units } \left[\frac{1}{pix^2}, \frac{1}{pix^4}\right]. \tag{3.46}$$

At this point, the camera measurement is simply given as an undistorted x and y pixel location. The measurement should be expressed next as a line-of-sight vector, or the vector from the focal point of the camera to the pixel location. This is given in the $\mathscr{F}$-frame as

$$\tilde{\bar{l}}^{\mathscr{F}} = \begin{bmatrix} l_x^{\mathscr{F}} \\ l_y^{\mathscr{F}} \\ l_z^{\mathscr{F}} \end{bmatrix} \tag{3.47}$$

$$\tilde{\bar{l}}^{\mathscr{F}} = C_{\mathscr{X}}^{\mathscr{F}} \begin{bmatrix} x_u \\ y_u \\ -f \end{bmatrix}. \tag{3.48}$$

Finally, this LOS vector can be used to create the same measurement as that used by Wu et. al. [7]:

$$\tilde{\bar{z}} = \begin{bmatrix} \frac{l_y^{\mathscr{F}}}{l_x^{\mathscr{F}}} \\ \frac{l_z^{\mathscr{F}}}{l_x^{\mathscr{F}}} \end{bmatrix}. \tag{3.49}$$

3.5 State Estimation

Given these sensor models and their resulting data, equations can be derived which more directly translate into vehicle state estimation. However, real-world sensors are imperfect. Sensors by themselves must be believed, but what happens when sensors start to disagree with each other? For example, what if integrating accelerometer and gyroscope information to get position information gives increasingly different results than GPS measurements? Fortunately, sensor manufacturers give a measure of how accurate each sensor can be trusted to be. Given models of the system dynamics and sensors, having

the measurement noise parameters of each sensor allows the sensor data to be intelligently combined in an extended Kalman filter (EKF). The filter then produces estimates of the specified states as well as a measure of how confident it is in its estimations.

This work employs a continuous-discrete EKF to combine sensor data intelligently to form its estimates. The filter is a continuous-discrete filter because it takes continuous dynamics models and produces discrete state estimates. Kalman filters have two basic steps: propagation via inertial sensors and updates via aiding sensors. Both steps are discussed in more detail in their respective subsections.

This section defines which states the filter estimates, describes the filter propagation and update steps, and defines the equations specific to this application that are used by each step. It is appropriate at this point to clarify the difference in notation between true (noiseless) variables, measurements produced by sensors, and quantities that are estimated by the EKF. An arbitrary variable, a, is considered a sensor-measured value if it is written as $\hat{a}$. That same variable is interpreted as an estimated value if it is written as $\tilde{a}$. It is considered a true, noiseless value if it is written simply as a. Please refer to the Math Notation page at the beginning of this work for more details.

3.5.1 Filter States

The first question to answer when setting up an EKF is, "Which states will the filter estimate?" This question depends on which states have equations that are functions of input sensor data. The filter for this work estimates position, velocity, and attitude states, but not attitude rate. The filter state vector is defined as

$$\hat{\bar{x}} = \begin{bmatrix} \hat{p}_n^{\mathscr{I}} \\ \hat{p}_e^{\mathscr{I}} \\ \hat{p}_d^{\mathscr{I}} \\ \hat{v}_n^{\mathscr{I}} \\ \hat{v}_e^{\mathscr{I}} \\ \hat{v}_d^{\mathscr{I}} \\ \hat{\phi} \\ \hat{\theta} \\ \hat{\psi} \end{bmatrix}. \tag{3.50}$$

Other variables of interest include the covariance for each state. Covariance values are what give the measure of estimation confidence mentioned earlier. This concept is explained in greater detail later in this work, but it is important to note that it was recorded from the equations in the following subsection when the filter was run.

3.5.2 Filter Propagation

The beginning states are usually reasonably well known. However, as time progresses, the estimated vehicle states must be propagated forward. Accelerometer and gyroscope measurements from the IMU allow the Kalman filter to do so. In a continuous-discrete Kalman filter, the propagation step computes the following general-form terms for each IMU sample in the order they appear here.

1. Propagate the states using the dynamics model, $\dot{\hat{\bar{x}}}(\hat{x}, u)$ which is a function of the most current filter states and the IMU sensor measurements:

$$\hat{\bar{x}}^+ = \hat{\bar{x}}^- + \left(\frac{T_{out}}{N}\right)\left(\dot{\hat{\bar{x}}}\left(\hat{\bar{x}}^-, \bar{u}\right)\right) \tag{3.51}$$

2. Compute the gradient matrix, A, evaluated with $\hat{\hat{x}}$ and u:

$$A = \left.\frac{\partial \dot{\hat{\hat{x}}}}{\partial \hat{\hat{x}}}\right|_{\hat{\hat{x}}^+, u} \tag{3.52}$$

3. Propagate the covariance matrix, P:

$$P = P + \left(\frac{T_{out}}{N}\right)\left(AP + PA^T + GQG^T\right) \tag{3.53}$$

Some definitions are required to apply this work's application to these three steps. The state models as a function of IMU data (accelerations and angular rates) and other states are

$$\dot{\hat{\hat{x}}}\left(\hat{\hat{x}}, \bar{u}\right) = \begin{bmatrix} \hat{\hat{v}}^{\mathscr{I}} \\ \bar{a}_g^{\mathscr{I}} + C_{\mathscr{B}}^{\mathscr{I}} \tilde{\tilde{a}}^{\mathscr{B}} \\ \hat{R}_{gyro}^{zyx} \tilde{\tilde{\omega}}_{gyro}^{\mathscr{B}} \end{bmatrix} \tag{3.54}$$

where $\tilde{\tilde{a}}^{\mathscr{B}}$ is the measured acceleration from the accelerometers expressed in the $\mathscr{B}$-frame, $\tilde{\tilde{\omega}}_{gyro}^{\mathscr{B}}$ is the vector of measured angular rates from the gyroscopes expressed in the $\mathscr{B}$-frame, and the matrix, $\hat{R}_{gyro}^{zyx}$, that relates angular rates to roll, pitch, and yaw is defined as

$$\hat{R}_{gyro}^{zyx} = \begin{bmatrix} 1 & \sin\left(\hat{\phi}\right)\tan\left(\theta\right) & \cos\left(\hat{\phi}\right)\tan\left(\theta\right) \\ 0 & \cos\left(\hat{\phi}\right) & -\sin\left(\hat{\phi}\right) \\ 0 & \sin\left(\hat{\phi}\right)\sec\left(\theta\right) & \cos\left(\hat{\phi}\right)\sec\left(\theta\right) \end{bmatrix}. \tag{3.55}$$

Noting that this vehicle's system causes no accelerations in the $\mathscr{B}$-frame's x or y directions, $\dot{\hat{\hat{x}}}$ can be re-written as

$$\dot{\hat{\hat{x}}}\left(\hat{\hat{x}},\bar{u}\right) = \begin{bmatrix} \begin{bmatrix} \hat{v}_n^{\mathscr{I}} \\ \hat{v}_e^{\mathscr{I}} \\ \hat{v}_d^{\mathscr{I}} \end{bmatrix} \\ \begin{bmatrix} 0 \\ 0 \\ g \end{bmatrix} + \begin{bmatrix} c\hat{\theta}c\hat{\psi} & s\hat{\phi}s\hat{\theta}c\hat{\psi} - c\hat{\phi}s\hat{\psi} & c\hat{\phi}s\hat{\theta}c\hat{\psi} + s\hat{\phi}s\hat{\psi} \\ c\hat{\theta}s\hat{\psi} & s\hat{\phi}s\hat{\theta}s\hat{\psi} + c\hat{\phi}c\hat{\psi} & c\hat{\phi}s\hat{\theta}s\hat{\psi} - s\hat{\phi}c\hat{\psi} \\ -s\hat{\theta} & s\hat{\phi}c\hat{\theta} & c\hat{\phi}c\hat{\theta} \end{bmatrix} \begin{bmatrix} 0 \\ 0 \\ \tilde{a}_z^{\mathscr{B}} \end{bmatrix} \\ \begin{bmatrix} 1 & \sin\left(\hat{\phi}\right)\tan\left(\hat{\theta}\right) & \cos\left(\hat{\phi}\right)\tan\left(\hat{\theta}\right) \\ 0 & \cos\left(\hat{\phi}\right) & -\sin\left(\hat{\phi}\right) \\ 0 & \sin\left(\hat{\phi}\right)\sec\left(\hat{\theta}\right) & \cos\left(\hat{\phi}\right)\sec\left(\hat{\theta}\right) \end{bmatrix} \begin{bmatrix} \tilde{\omega}_p^{\mathscr{B}} \\ \tilde{\omega}_q^{\mathscr{B}} \\ \tilde{\omega}_r^{\mathscr{B}} \end{bmatrix} \end{bmatrix} \tag{3.56}$$

$$= \begin{bmatrix} \hat{v}_n^{\mathscr{I}} \\ \hat{v}_e^{\mathscr{I}} \\ \hat{v}_d^{\mathscr{I}} \\ \begin{bmatrix} \left(c\hat{\phi}s\hat{\theta}c\hat{\psi} + s\hat{\phi}s\hat{\psi}\right)\tilde{a}_z^{\mathscr{B}} \\ \left(c\hat{\phi}s\hat{\theta}s\hat{\psi} - s\hat{\phi}c\hat{\psi}\right)\tilde{a}_z^{\mathscr{B}} \\ g + \left(c\hat{\phi}c\hat{\theta}\right)\tilde{a}_z^{\mathscr{B}} \end{bmatrix} \\ \begin{bmatrix} \tilde{\omega}_p^{\mathscr{B}} + \tilde{\omega}_q^{\mathscr{B}}\left(\sin\left(\hat{\phi}\right)\tan\left(\hat{\theta}\right)\right) + \tilde{\omega}_r^{\mathscr{B}}\left(\cos\left(\hat{\phi}\right)\tan\left(\hat{\theta}\right)\right) \\ \tilde{\omega}_q^{\mathscr{B}}\left(\cos\left(\hat{\phi}\right)\right) + \tilde{\omega}_r^{\mathscr{B}}\left(-\sin\left(\hat{\phi}\right)\right) \\ \tilde{\omega}_q^{\mathscr{B}}\left(\sin\left(\hat{\phi}\right)\sec\left(\hat{\theta}\right)\right) + \tilde{\omega}_r^{\mathscr{B}}\left(\cos\left(\hat{\phi}\right)\sec\left(\hat{\theta}\right)\right) \end{bmatrix} \end{bmatrix} \tag{3.57}$$

$$= \begin{bmatrix} \hat{v}_x^{\mathcal{I}} \\ \hat{v}_y^{\mathcal{I}} \\ \hat{v}_z^{\mathcal{I}} \\ \left(\cos\hat{\phi}\sin\hat{\theta}\cos\hat{\psi} + \sin\hat{\phi}\sin\hat{\psi}\right)\tilde{a}_z \\ \left(\cos\hat{\phi}\sin\hat{\theta}\sin\hat{\psi} - \sin\hat{\phi}\cos\hat{\psi}\right)\tilde{a}_z \\ g + \left(\cos\hat{\phi}\cos\hat{\theta}\right)\tilde{a}_z \\ \tilde{\omega}_p + \tilde{\omega}_q\sin\hat{\phi}\tan\hat{\theta} + \tilde{\omega}_r\cos\hat{\phi}\tan\hat{\theta} \\ \tilde{\omega}_q\cos\hat{\phi} - \tilde{\omega}_r\sin\hat{\phi} \\ \tilde{\omega}_q\sin\hat{\phi}\sec\hat{\theta} + \tilde{\omega}_r\cos\hat{\phi}\sec\hat{\theta} \end{bmatrix}. \tag{3.58}$$

It then follows that the A matrix is

$$A = \begin{bmatrix} 0 & 0 & 0 & 1 & 0 & 0 & 0 & 0 & 0 \\ 0 & 0 & 0 & 0 & 1 & 0 & 0 & 0 & 0 \\ 0 & 0 & 0 & 0 & 0 & 1 & 0 & 0 & 0 \\ 0 & 0 & 0 & 0 & 0 & 0 & \frac{\partial\dot{\hat{x}}_4}{\partial\hat{\phi}} & \frac{\partial\dot{\hat{x}}_4}{\partial\hat{\theta}} & \frac{\partial\dot{\hat{x}}_4}{\partial\hat{\psi}} \\ 0 & 0 & 0 & 0 & 0 & 0 & \frac{\partial\dot{\hat{x}}_5}{\partial\hat{\phi}} & \frac{\partial\dot{\hat{x}}_5}{\partial\hat{\theta}} & \frac{\partial\dot{\hat{x}}_5}{\partial\hat{\psi}} \\ 0 & 0 & 0 & 0 & 0 & 0 & \frac{\partial\dot{\hat{x}}_6}{\partial\hat{\phi}} & \frac{\partial\dot{\hat{x}}_6}{\partial\hat{\theta}} & 0 \\ 0 & 0 & 0 & 0 & 0 & 0 & \frac{\partial\dot{\hat{x}}_7}{\partial\hat{\phi}} & \frac{\partial\dot{\hat{x}}_7}{\partial\hat{\theta}} & 0 \\ 0 & 0 & 0 & 0 & 0 & 0 & \frac{\partial\dot{\hat{x}}_8}{\partial\hat{\phi}} & 0 & 0 \\ 0 & 0 & 0 & 0 & 0 & 0 & \frac{\partial\dot{\hat{x}}_9}{\partial\hat{\phi}} & \frac{\partial\dot{\hat{x}}_9}{\partial\hat{\theta}} & 0 \end{bmatrix} \tag{3.59}$$

where

$$\frac{\partial\dot{\hat{x}}_4}{\partial\hat{\phi}} = \left(-\sin\hat{\phi}\sin\hat{\theta}\cos\hat{\psi} + \cos\hat{\phi}\sin\hat{\psi}\right)\tilde{a}_z \tag{3.60}$$

$$\frac{\partial\dot{\hat{x}}_4}{\partial\hat{\theta}} = \left(\cos\hat{\phi}\cos\hat{\theta}\cos\hat{\psi}\right)\tilde{a}_z \tag{3.61}$$

$$\frac{\partial\dot{\hat{x}}_4}{\partial\hat{\psi}} = \left(-\cos\hat{\phi}\sin\hat{\theta}\sin\hat{\psi} + \sin\hat{\phi}\cos\hat{\psi}\right)\tilde{a}_z \tag{3.62}$$

$$\frac{\partial\dot{\hat{x}}_5}{\partial\hat{\phi}} = \left(-\sin\hat{\phi}\sin\hat{\theta}\sin\hat{\psi} - \cos\hat{\phi}\cos\hat{\psi}\right)\tilde{a}_z \tag{3.63}$$

$$\frac{\partial \dot{\hat{x}}_5}{\partial \hat{\theta}} = \left(\cos\hat{\phi}\cos\hat{\theta}\sin\hat{\psi}\right)\tilde{a}_z \tag{3.64}$$

$$\frac{\partial \dot{\hat{x}}_5}{\partial \hat{\psi}} = \left(\cos\hat{\phi}\sin\hat{\theta}\cos\hat{\psi} + \sin\hat{\phi}\sin\hat{\psi}\right)\tilde{a}_z \tag{3.65}$$

$$\frac{\partial \dot{\hat{x}}_6}{\partial \hat{\phi}} = \left(-\sin\hat{\phi}\cos\hat{\theta}\right)\tilde{a}_z \tag{3.66}$$

$$\frac{\partial \dot{\hat{x}}_6}{\partial \hat{\theta}} = \left(-\cos\hat{\phi}\sin\hat{\theta}\right)\tilde{a}_z \tag{3.67}$$

$$\frac{\partial \dot{\hat{x}}_7}{\partial \hat{\phi}} = \tilde{\omega}_q\left(\cos\hat{\phi}\tan\hat{\theta}\right) + \tilde{\omega}_r\left(-\sin\hat{\phi}\tan\hat{\theta}\right) \tag{3.68}$$

$$\frac{\partial \dot{\hat{x}}_7}{\partial \hat{\theta}} = \left(\tilde{\omega}_q\sin\hat{\phi} + \tilde{\omega}_r\cos\hat{\phi}\right)\sec^2\hat{\theta} \tag{3.69}$$

$$\frac{\partial \dot{\hat{x}}_8}{\partial \hat{\phi}} = \tilde{\omega}_q\left(-\sin\hat{\phi}\right) + \tilde{\omega}_r\left(-\cos\hat{\phi}\right) \tag{3.70}$$

$$\frac{\partial \dot{\hat{x}}_9}{\partial \hat{\phi}} = \left(\tilde{\omega}_q\cos\hat{\phi} + \tilde{\omega}_r\left(-\sin\hat{\phi}\right)\right)\sec\hat{\theta} \tag{3.71}$$

$$\frac{\partial \dot{\hat{x}}_9}{\partial \hat{\theta}} = \left(\tilde{\omega}_q\left(-\sin\hat{\phi}\right) + \tilde{\omega}_r\left(-\cos\phi\right)\right)\tan\hat{\theta}\sec\hat{\theta}. \tag{3.72}$$

The matrix, Q, contains information about the process noise. The strength of the process noise is defined by the IMU sensors' accuracy:

$$Q = \begin{bmatrix} \sigma_{a_x}^2 & 0 & 0 & 0 & 0 & 0 \\ 0 & \sigma_{a_y}^2 & 0 & 0 & 0 & 0 \\ 0 & 0 & \sigma_{a_z}^2 & 0 & 0 & 0 \\ 0 & 0 & 0 & \sigma_{\omega_x}^2 & 0 & 0 \\ 0 & 0 & 0 & 0 & \sigma_{\omega_y}^2 & 0 \\ 0 & 0 & 0 & 0 & 0 & \sigma_{\omega_z}^2 \end{bmatrix} \tag{3.73}$$

where σ_{a_x}, σ_{a_y}, and σ_{a_z} are the standard deviations of the accelerometer noise in the x, y, and z directions respectively, and σ_{ω_x}, σ_{ω_y}, and σ_{ω_z} are the standard deviations of the gyroscope noise about the x, y, and z-axes.

Finally, the G matrix, which projects the IMU sensor noise into the states, is defined as

$$G = \begin{bmatrix} 0 & 0 & 0 & 0 & 0 & 0 \\ 0 & 0 & 0 & 0 & 0 & 0 \\ 0 & 0 & 0 & 0 & 0 & 0 \\ 0 & 0 & \cos(\phi)\sin(\theta) & 0 & 0 & 0 \\ 0 & 0 & -\sin(\phi) & 0 & 0 & 0 \\ 0 & 0 & \cos(\phi)\cos(\theta) & 0 & 0 & 0 \\ 0 & 0 & 0 & 1 & \sin(\phi)\tan(\theta) & \cos(\phi)\tan(\theta) \\ 0 & 0 & 0 & 0 & \cos(\phi) & -\sin(\phi) \\ 0 & 0 & 0 & 0 & \sin(\phi)\sec(\theta) & \cos(\phi)\sec(\theta) \end{bmatrix}. \tag{3.74}$$

These propagation equations are run at the frequency of the IMU samples. For this work, the IMU frequency is 150 Hz.

3.5.3 General EKF Updates

The general equations for a continuous-discrete Kalman filter are set forth here. Recall that accelerometers and gyroscopes, as part of the IMU, are being used in a dynamic model replacement mode. Their measurements, as described above, are essentially integrated into the propagation step. The update step in a Kalman filter only operates on aiding sensors. A given system can have several aiding sensors including, but not limited to GPS and cameras. If a system has n aiding sensors, let sensor i be any one of those aiding sensors. Each time the filter receives a measurement from sensor i, $\tilde{z}_i$, the filter applies the measurement update after a normal propagation by computing the following equations in order:

1. Predict the expected measurement:

$$\hat{z}_i = h_i\left(\hat{\bar{x}}\right) \tag{3.75}$$

2. Compute the measurement geometry matrix, H_i, which projects the sensor measurement into the filter states:

$$H_i\left(\hat{\hat{x}}\right) = \left.\frac{\partial h_i\left(\hat{\hat{x}}\right)}{\partial \hat{\hat{x}}}\right|_{\hat{\hat{x}}} \tag{3.76}$$

3. Compute the residual covariance matrix, $\mathcal{R}$:

$$\mathcal{R} = H_i P^- H_i^T + R_i \tag{3.77}$$

where R_i is the measurement noise matrix which is made from the standard deviation of the sensor.

4. Compute the Kalman gain matrix, K_i:

$$K_i = P^- H_i^T R^{-1} \tag{3.78}$$

5. Update the states using a Kalman-weighted measurement residual:

$$\hat{\hat{x}}^+ = \hat{\hat{x}}^- + K_i\left(\tilde{z}_i - \hat{z}_i\right) \tag{3.79}$$

6. Update the state covariance using Joseph's form of the update:

$$P^+ = \left(I - K_i H_i\right) P^- \left(I - K_i H_i\right)^T + K_i R_i K_i^T \tag{3.80}$$

These equations are applied to both GPS and LOS measurements in the next two sections of this work. To clarify, each trajectory was run once with GPS measurements enabled and LOS measurements disabled. Then, GPS measurements were disabled and LOS measurements were enabled for every combination of trajectory and apparent landmark density. The variables in the equations above are defined for GPS and LOS measurements in the following subsections.

3.5.4 GPS Measurement Update Equations

A baseline Kalman filter performance is needed for the purpose of this work. GPS

measurements are implemented to fill this capacity because GPS-aided navigation is very well characterized relative to image-aided navigation.

There are only three variables from the general equations in the preceding subsection that need to be defined for each measurement. The first is, $\hat{\bar{z}}_\gamma$, which is comprised of a set of equations which give the expected GPS measurements:

$$\hat{\bar{z}}_\gamma = \begin{bmatrix} \hat{p}_n^{\mathscr{I}} \\ \hat{p}_e^{\mathscr{I}} \\ -\hat{p}_d^{\mathscr{I}} \\ \hat{v}_n^{\mathscr{I}} \\ \hat{v}_e^{\mathscr{I}} \\ -\hat{v}_d^{\mathscr{I}} \end{bmatrix}. \tag{3.81}$$

Note that the third position and velocity states in the filter are defined as a downward direction with respect to the $\mathscr{I}$-frame origin expressed in the $\mathscr{I}$-frame, while the GPS measurements define them as height or upward direction with respect to and expressed in the same frame.

Next, the measurement geometry matrix for GPS updates is derived to be

$$H_{GPS} = \begin{bmatrix} 1 & 0 & 0 & 0 & 0 & 0 & 0 & 0 & 0 \\ 0 & 1 & 0 & 0 & 0 & 0 & 0 & 0 & 0 \\ 0 & 0 & 1 & 0 & 0 & 0 & 0 & 0 & 0 \\ 0 & 0 & 0 & 1 & 0 & 0 & 0 & 0 & 0 \\ 0 & 0 & 0 & 0 & 1 & 0 & 0 & 0 & 0 \\ 0 & 0 & 0 & 0 & 0 & 1 & 0 & 0 & 0 \end{bmatrix}. \tag{3.82}$$

Finally, the measurement noise matrix for GPS updates, R_{GPS}, is defined as

$$R_{GPS} = \begin{bmatrix} \sigma^2_{\gamma_{p_n}} & 0 & 0 & 0 & 0 & 0 \\ 0 & \sigma^2_{\gamma_{p_e}} & 0 & 0 & 0 & 0 \\ 0 & 0 & \sigma^2_{\gamma_{p_h}} & 0 & 0 & 0 \\ 0 & 0 & 0 & \sigma^2_{\gamma_{v_n}} & 0 & 0 \\ 0 & 0 & 0 & 0 & \sigma^2_{\gamma_{v_e}} & 0 \\ 0 & 0 & 0 & 0 & 0 & \sigma^2_{\gamma_{v_h}} \end{bmatrix} \tag{3.83}$$

where $\sigma_{\gamma_{p_n}}$, $\sigma_{\gamma_{p_e}}$, $\sigma_{\gamma_{p_h}}$, $\sigma_{\gamma_{v_n}}$, $\sigma_{\gamma_{v_e}}$, and $\sigma_{\gamma_{v_h}}$ are the standard deviations of the GPS position and velocity noise in the north, east, and up directions.

3.5.5 LOS Measurement Updates Equations

The same variables need to be estimated for image-aided navigation using LOS measurements. Each time the image sensor produces an image frame, the filter must complete an update step for each landmark detected in the frame. Therefore, the following definitions and equations apply to each detected landmark in turn for a given image.

First, the relative position of the landmark with respect to the $\mathscr{F}$-frame, $\hat{\bar{r}}^{\mathscr{F}}_{L/\mathscr{F}}$, must be predicted. The relative position vector can be predicted in place of predicting the LOS vector measured by the camera (defined as the pixel position relative to the focal point of the camera) because the final version of the predicted measurement yields the same ratio as that of the final version of the actual measurement if they point in the same direction. Magnitudes do not matter because both vectors form similar right triangles. The prediction of $\hat{\bar{r}}^{\mathscr{F}}_{L/\mathscr{F}}$ is given as

$$\hat{\bar{r}}^{\mathscr{F}}_{L/\mathscr{F}} = \bar{p}^{\mathscr{F}}_{L} - \hat{\bar{p}}^{\mathscr{F}} \tag{3.84}$$

$$= C^{\mathscr{F}}_{\mathscr{B}} \hat{C}^{\mathscr{B}}_{\mathscr{V}} C^{\mathscr{V}}_{\mathscr{I}} \bar{p}^{\mathscr{I}}_{L} - C^{\mathscr{F}}_{\mathscr{B}} \hat{C}^{\mathscr{B}}_{\mathscr{V}} C^{\mathscr{V}}_{\mathscr{I}} \hat{\bar{p}}^{\mathscr{I}} \tag{3.85}$$

$$= C^{\mathscr{F}}_{\mathscr{B}} \hat{C}^{\mathscr{B}}_{\mathscr{V}} C^{\mathscr{V}}_{\mathscr{I}} \left(\bar{p}^{\mathscr{I}}_{L} - \hat{\bar{p}}^{\mathscr{I}} \right) \tag{3.86}$$

$$= \begin{bmatrix} \hat{r}^{\mathscr{F}}_{L/\mathscr{F},x} \\ \hat{r}^{\mathscr{F}}_{L/\mathscr{F},y} \\ \hat{r}^{\mathscr{F}}_{L/\mathscr{F},z} \end{bmatrix} \tag{3.87}$$

where $\bar{p}^{\mathscr{F}}_{L}$ is the known position of the landmark with respect to the $\mathscr{I}$-frame origin and $\hat{\bar{p}}^{\mathscr{I}}$ is the filter's estimate of the position states, as previously indicated. The actual LOS measurement prediction is defined as the two-dimensional vector

$$\hat{\bar{z}}_{\lambda} = \begin{bmatrix} \frac{\hat{r}^{\mathscr{F}}_{L/\mathscr{F},y}}{\hat{r}^{\mathscr{F}}_{L/\mathscr{F},x}} \\ \frac{\hat{r}^{\mathscr{F}}_{L/\mathscr{F},z}}{\hat{r}^{\mathscr{F}}_{L/\mathscr{F},x}} \end{bmatrix}. \tag{3.88}$$

Noting that

$$\hat{\bar{\alpha}} = \begin{bmatrix} \hat{\phi} \\ \hat{\theta} \\ \hat{\psi} \end{bmatrix} \tag{3.89}$$

the measurement geometry matrix for LOS measurements, H_{λ} is defined as

$$H_{\lambda} = \left.\frac{\partial \hat{\bar{z}}_{\lambda}}{\partial \hat{\bar{x}}}\right|_{\hat{\bar{x}}} = \left.\begin{bmatrix} \frac{\partial \hat{\bar{z}}_{\lambda}}{\partial \hat{\bar{p}}^{\mathscr{I}}} & \frac{\partial \hat{\bar{z}}_{\lambda}}{\partial \hat{\bar{v}}^{\mathscr{I}}} & \frac{\partial \hat{\bar{z}}_{\lambda}}{\partial \hat{\bar{\alpha}}} \end{bmatrix}\right|_{\hat{\bar{x}}}. \tag{3.90}$$

In order to derive the partial derivatives that make up the terms of H_{λ}, defining a new variable, Λ, allows for some notational brevity later on:

$$\Lambda = \frac{\partial \hat{\bar{z}}_{\lambda}}{\partial \hat{\bar{l}}^{\mathscr{F}}} = \begin{bmatrix} \frac{-\hat{r}^{\mathscr{F}}_{L/\mathscr{F},y}}{\left(\hat{r}^{\mathscr{F}}_{L/\mathscr{F},x}\right)^2} & \frac{1}{\hat{r}^{\mathscr{F}}_{L/\mathscr{F},x}} & 0 \\ \frac{-\hat{r}^{\mathscr{F}}_{L/\mathscr{F},z}}{\left(\hat{r}^{\mathscr{F}}_{L/\mathscr{F},x}\right)^2} & 0 & \frac{1}{\hat{r}^{\mathscr{F}}_{L/\mathscr{F},x}} \end{bmatrix}. \tag{3.91}$$

Solving for the terms relative to vehicle position yields

$$\frac{\partial \hat{\bar{z}}_{\lambda}}{\partial \hat{\bar{p}}} = \left(\frac{\partial \hat{\bar{z}}_{\lambda}}{\partial \hat{\bar{r}}^{\mathscr{F}}_{L/\mathscr{F}}}\right)\left(\frac{\partial \hat{\bar{r}}^{\mathscr{F}}_{L/\mathscr{F}}}{\partial \hat{\bar{p}}^{\mathscr{I}}}\right) \tag{3.92}$$

$$= \Lambda \left(\frac{C_{\mathscr{B}}^{\mathscr{F}} \hat{C}_{\mathscr{V}}^{\mathscr{B}} C_{\mathscr{J}}^{\mathscr{V}} \partial \hat{\bar{r}}_{L/\mathscr{F}}^{\mathscr{J}}}{\partial \hat{\bar{p}}^{\mathscr{J}}} \right) \tag{3.93}$$

$$= \Lambda C_{\mathscr{B}}^{\mathscr{F}} \hat{C}_{\mathscr{V}}^{\mathscr{B}} C_{\mathscr{J}}^{\mathscr{V}} \left(\frac{\partial \hat{\bar{r}}_{L/\mathscr{F}}^{\mathscr{J}}}{\partial \hat{\bar{p}}^{\mathscr{J}}} \right) \tag{3.94}$$

$$= \Lambda \hat{C}_{\mathscr{J}}^{\mathscr{F}} \left(\frac{\partial \left(\bar{p}_L^{\mathscr{J}} - \hat{\bar{p}}^{\mathscr{J}} \right)}{\partial \hat{\bar{p}}^{\mathscr{J}}} \right) \tag{3.95}$$

$$= \Lambda \hat{C}_{\mathscr{J}}^{\mathscr{F}} \left(-I_{3x3} \right) \tag{3.96}$$

$$= -\Lambda \hat{C}_{\mathscr{J}}^{\mathscr{F}}. \tag{3.97}$$

For use later in this work, this term is defined as

$$H_{pos} = -\Lambda \hat{C}_{\mathscr{J}}^{\mathscr{F}}. \tag{3.98}$$

Solving for the terms relative to vehicle velocity yields

$$\frac{\partial \hat{\bar{z}}_\lambda}{\partial \hat{\bar{v}}} = \left(\frac{\partial \hat{\bar{z}}_\lambda}{\partial \hat{\bar{l}}^{\mathscr{F}}} \right) \left(\frac{\partial \hat{\bar{r}}_{L/\mathscr{F}}^{\mathscr{F}}}{\partial \hat{\bar{v}}^{\mathscr{J}}} \right) \tag{3.99}$$

$$= \Lambda 0_{3x3} \tag{3.100}$$

$$= 0_{2x3}. \tag{3.101}$$

Both the position and velocity partial derivatives match the results obtained by Wu et. al., but their filter state vector defines the attitude states as a quaternion vector [7]. However, the attitude states in this work are stored as Euler angles. Therefore, the final partial derivative is re-derived for this work here:

$$\frac{\partial \hat{\bar{z}}_\lambda}{\partial \hat{\bar{\alpha}}} = \left(\frac{\partial \hat{\bar{z}}_\lambda}{\partial \hat{\bar{r}}_{L/\mathscr{F}}^{\mathscr{F}}} \right) \left(\frac{\partial \hat{\bar{r}}_{L/\mathscr{F}}^{\mathscr{F}}}{\partial \hat{\bar{\alpha}}} \right) \tag{3.102}$$

$$= \Lambda C_{\mathscr{B}}^{\mathscr{F}} \left(\frac{\partial \left(\hat{C}_{\mathscr{V}}^{\mathscr{B}} C_{\mathscr{J}}^{\mathscr{V}} \hat{\bar{r}}_{L/\mathscr{F}}^{\mathscr{J}} \right)}{\partial \hat{\bar{\alpha}}} \right) \tag{3.103}$$

$$= \Lambda C_{\mathscr{B}}^{\mathscr{F}} \left(\frac{\partial \left(\hat{C}_{\mathscr{V}}^{\mathscr{B}} C_{\mathscr{J}}^{\mathscr{V}} \left(\bar{p}_f^{\mathscr{J}} - \hat{\bar{p}}^{\mathscr{J}} \right) \right)}{\partial \hat{\bar{\alpha}}} \right). \tag{3.104}$$

To solve for $\frac{\partial\left(\hat{C}_{\mathscr{V}}^{\mathscr{B}} C_{\mathscr{J}}^{\mathscr{V}} \hat{\bar{r}}_{L/\mathscr{F}}^{\mathscr{J}}\right)}{\partial \hat{\bar{\alpha}}}$, the $\hat{C}_{\mathscr{V}}^{\mathscr{B}} C_{\mathscr{J}}^{\mathscr{V}} \hat{\bar{r}}_{L/\mathscr{F}}^{\mathscr{J}}$ term is written out as

$$\hat{C}_{\mathscr{V}}^{\mathscr{B}} C_{\mathscr{J}}^{\mathscr{V}} \hat{\bar{r}}_{L/\mathscr{F}}^{\mathscr{J}} = \begin{bmatrix} c\hat{\theta}c\hat{\psi} & c\hat{\theta}s\hat{\psi} & -s\hat{\theta} \\ s\hat{\phi}s\hat{\theta}c\hat{\psi} - c\hat{\phi}s\hat{\psi} & s\hat{\phi}s\hat{\theta}s\hat{\psi} + c\hat{\phi}c\hat{\psi} & s\hat{\phi}c\hat{\theta} \\ c\hat{\phi}s\hat{\theta}c\hat{\psi} + s\hat{\phi}s\hat{\psi} & c\hat{\phi}s\hat{\theta}s\hat{\psi} - s\hat{\phi}c\hat{\psi} & c\hat{\phi}c\hat{\theta} \end{bmatrix} \begin{bmatrix} 1 & 0 & 0 \\ 0 & 1 & 0 \\ 0 & 0 & 1 \end{bmatrix} \begin{bmatrix} \hat{\bar{r}}_{L/\mathscr{F},x}^{\mathscr{J}} \\ \hat{\bar{r}}_{L/\mathscr{F},y}^{\mathscr{J}} \\ \hat{\bar{r}}_{L/\mathscr{F},z}^{\mathscr{J}} \end{bmatrix} \tag{3.105}$$

$$\begin{bmatrix} \hat{\bar{r}}_{L/\mathscr{F},x}^{\mathscr{B}} \\ \hat{\bar{r}}_{L/\mathscr{F},y}^{\mathscr{B}} \\ \hat{\bar{r}}_{L/\mathscr{F},z}^{\mathscr{B}} \end{bmatrix} = \begin{bmatrix} \hat{\bar{r}}_{L/\mathscr{F},x}^{\mathscr{J}} \left(c\hat{\theta}c\hat{\psi}\right) + \hat{\bar{r}}_{L/\mathscr{F},y}^{\mathscr{J}} \left(c\hat{\theta}s\hat{\psi}\right) + \hat{\bar{r}}_{L/\mathscr{F},z}^{\mathscr{J}} \left(-s\hat{\theta}\right) \\ \hat{\bar{r}}_{L/\mathscr{F},x}^{\mathscr{J}} \left(s\hat{\phi}s\hat{\theta}c\hat{\psi} - c\hat{\phi}s\hat{\psi}\right) + \hat{\bar{r}}_{L/\mathscr{F},y}^{\mathscr{J}} \left(s\hat{\phi}s\hat{\theta}s\hat{\psi} + c\hat{\phi}c\hat{\psi}\right) + \hat{\bar{r}}_{L/\mathscr{F},z}^{\mathscr{J}} \left(s\hat{\phi}c\hat{\theta}\right) \\ \hat{\bar{r}}_{L/\mathscr{F},x}^{\mathscr{J}} \left(c\hat{\phi}s\hat{\theta}c\hat{\psi} + s\hat{\phi}s\hat{\psi}\right) + \hat{\bar{r}}_{L/\mathscr{F},y}^{\mathscr{J}} \left(c\hat{\phi}s\hat{\theta}s\hat{\psi} - s\hat{\phi}c\hat{\psi}\right) + \hat{\bar{r}}_{L/\mathscr{F},z}^{\mathscr{J}} \left(c\hat{\phi}c\hat{\theta}\right) \end{bmatrix} \tag{3.106}$$

where

$$c\hat{\phi} = \cos\hat{\phi} \tag{3.107}$$

$$c\hat{\theta} = \cos\hat{\theta} \tag{3.108}$$

$$c\hat{\psi} = \cos\hat{\psi} \tag{3.109}$$

$$s\hat{\phi} = \sin\hat{\phi} \tag{3.110}$$

$$s\hat{\theta} = \sin\hat{\theta} \tag{3.111}$$

$$s\hat{\psi} = \sin\hat{\psi}. \tag{3.112}$$

From here, the partial derivative term becomes the following 3×3 matrix

$$\frac{\partial\left(\hat{C}_{\mathscr{V}}^{\mathscr{B}} C_{\mathscr{J}}^{\mathscr{V}} \hat{\bar{r}}_{L/\mathscr{F}}^{\mathscr{J}}\right)}{\partial \hat{\bar{\alpha}}} = \begin{bmatrix} L_{11} & L_{12} & L_{13} \\ L_{21} & L_{22} & L_{23} \\ L_{31} & L_{32} & L_{33} \end{bmatrix} \tag{3.113}$$

where

$$L_{11} = \frac{\partial \hat{\bar{r}}_{L/\mathscr{F},x}^{\mathscr{B}}}{\partial \hat{\phi}} \tag{3.114}$$

$$= 0 \tag{3.115}$$

$$L_{12} = \frac{\partial \hat{\bar{r}}^{\mathscr{B}}_{L/\mathscr{F},x}}{\partial \hat{\theta}} \tag{3.116}$$

$$= \hat{\bar{r}}^{\mathscr{B}}_{L/\mathscr{F},x}\left(-s\theta c\psi\right) + \hat{\bar{r}}^{\mathscr{B}}_{L/\mathscr{F},y}\left(-s\theta s\psi\right) + \hat{\bar{r}}^{\mathscr{B}}_{L/\mathscr{F},z}\left(-c\theta\right) \tag{3.117}$$

$$L_{13} = \frac{\partial \hat{\bar{r}}^{\mathscr{B}}_{L/\mathscr{F},x}}{\partial \hat{\psi}} \tag{3.118}$$

$$= \hat{\bar{r}}^{\mathscr{B}}_{L/\mathscr{F},x}\left(-c\theta s\psi\right) + \hat{\bar{r}}^{\mathscr{B}}_{L/\mathscr{F},y}\left(c\theta c\psi\right) \tag{3.119}$$

$$L_{21} = \frac{\partial \hat{\bar{r}}^{\mathscr{B}}_{L/\mathscr{F},y}}{\partial \hat{\phi}} \tag{3.120}$$

$$= \hat{\bar{r}}^{\mathscr{B}}_{L/\mathscr{F},x}\left(c\phi s\theta c\psi + s\phi s\psi\right) + \hat{\bar{r}}^{\mathscr{B}}_{L/\mathscr{F},y}\left(c\phi s\theta s\psi - s\phi c\psi\right) + \hat{\bar{r}}^{\mathscr{B}}_{L/\mathscr{F},z}\left(c\phi c\theta\right) \tag{3.121}$$

$$L_{22} = \frac{\partial \hat{\bar{r}}^{\mathscr{B}}_{L/\mathscr{F},y}}{\partial \hat{\theta}} \tag{3.122}$$

$$= \hat{\bar{r}}^{\mathscr{B}}_{L/\mathscr{F},x}\left(s\phi c\theta c\psi\right) + \hat{\bar{r}}^{\mathscr{B}}_{L/\mathscr{F},y}\left(s\phi c\theta s\psi\right) + \hat{\bar{r}}^{\mathscr{B}}_{L/\mathscr{F},z}\left(-s\phi s\theta\right) \tag{3.123}$$

$$L_{23} = \frac{\partial \hat{\bar{r}}^{\mathscr{B}}_{L/\mathscr{F},y}}{\partial \hat{\psi}} \tag{3.124}$$

$$= \hat{\bar{r}}^{\mathscr{B}}_{L/\mathscr{F},x}\left(-s\phi s\theta s\psi - c\phi c\psi\right) + \hat{\bar{r}}^{\mathscr{B}}_{L/\mathscr{F},y}\left(s\phi s\theta c\psi - c\phi s\psi\right) \tag{3.125}$$

$$L_{31} = \frac{\partial \hat{\bar{r}}^{\mathscr{B}}_{L/\mathscr{F},z}}{\partial \hat{\phi}} \tag{3.126}$$

$$= \hat{\bar{r}}^{\mathscr{B}}_{L/\mathscr{F},x}\left(-s\phi s\theta c\psi + c\phi s\psi\right) + \hat{\bar{r}}^{\mathscr{B}}_{L/\mathscr{F},y}\left(-s\phi s\theta s\psi - c\phi c\psi\right) + \hat{\bar{r}}^{\mathscr{B}}_{L/\mathscr{F},z}\left(-s\phi c\theta\right) \tag{3.127}$$

$$L_{32} = \frac{\partial \hat{\bar{r}}^{\mathscr{B}}_{L/\mathscr{F},z}}{\partial \hat{\theta}} \tag{3.128}$$

$$= \hat{\bar{r}}^{\mathscr{B}}_{L/\mathscr{F},x}\left(c\phi c\theta c\psi\right) + \hat{\bar{r}}^{\mathscr{B}}_{L/\mathscr{F},y}\left(c\phi c\theta s\psi\right) + \hat{\bar{r}}^{\mathscr{B}}_{L/\mathscr{F},z}\left(-c\phi s\theta\right) \tag{3.129}$$

$$L_{33} = \frac{\partial \hat{\bar{r}}^{\mathscr{B}}_{L/\mathscr{F},z}}{\partial \hat{\psi}} \tag{3.130}$$

$$= \hat{\bar{r}}^{\mathscr{B}}_{L/\mathscr{F},x}\left(-c\phi s\theta s\psi + s\phi c\psi\right) + \hat{\bar{r}}^{\mathscr{B}}_{L/\mathscr{F},y}\left(c\phi s\theta c\psi + s\phi s\psi\right). \tag{3.131}$$

The measurement noise matrix for LOS updates, R_λ is defined as

$$R_\lambda = \begin{bmatrix} \sigma^2_{\delta\lambda_x} & 0 \\ 0 & \sigma^2_{\delta\lambda_y} \end{bmatrix} \tag{3.132}$$

where $\sigma_{\delta\lambda_x}$ and $\sigma_{\delta\lambda_x}$ are the standard deviations of the camera x and y pixel measurement noise respectively.

CHAPTER 4

Results And Analysis

As stated in previous chapters, the questions addressed by this work deal with the relationships between trajectory shape, altitude, and the number of landmarks observed when using LOS measurements in image-aided navigation. Fig. 1.2 shows the overall setup by which these questions are addressed in this work. Section 3.1 details how this process was run to estimate vehicle states and produce filter covariance for all of the combinations of trajectory shapes, altitudes, and ALDs for GPS-aided and image-aided navigation solutions. This chapter discusses the presentation of that data, identifies several patterns, and then discusses the implications of these findings.

4.1 The Data

There are two main points to clarify about how the data presented below is to be interpreted. First, what exactly is plotted? And second, how is it organized? The following two subsections address these questions.

4.1.1 3σ Uncertainty Comparison

Since this work addresses questions concerning the effect of variables on how confident the filter is, only the covariance data is examined here. The square root of the diagonal terms of the EKF's resulting covariance matrix gives the standard deviation of the states:

$$\begin{bmatrix} \sigma_{p_n} \\ \sigma_{p_e} \\ \sigma_{p_d} \\ \sigma_{v_n} \\ \sigma_{v_e} \\ \sigma_{v_d} \\ \sigma_{\phi} \\ \sigma_{\theta} \\ \sigma_{\psi} \end{bmatrix}. \tag{4.1}$$

What do these quantities mean? The filter knows that its estimate states do not exactly equal the true states. However, it is statistically certain that each true state is almost always bounded by, or within three standard deviations, or 3σ, of its estimate. This work uses this 3σ measure of uncertainty as a comparison tool to discuss how much information the filter has been able to gain from its aiding sensor. The 3σ term can be referred to as either a confidence interval or uncertainty bounds, depending on context. Smaller 3σ values indicate that the filter is more confident in its solution. This implies that the aiding measurements had more information than if the 3σ values were large.

Recalling that GPS-aided solutions were run for each trajectory as a baseline, GPS-aided solution's 3σ values will be subtracted from the image-aided solution's 3σ values. This allows all the data presented below to be directly compared to GPS performance. If the 3σ values in any of the plots are negative, that means that the image-aided navigation solution had more information than the GPS-aided solution and was therefore more confident.

4.1.2 Data Organization

Trying to graphically observe and understand the relationships sought after by this work presents an interesting challenge. The data is five-dimensional. The information and confidence metric, 3σ, must be viewed against time. Then, this experiment intentionally varied three environmental variables: trajectory shape, attitude, and apparent landmark

density.

To address this issue and pursue the search for patterns that indicate a relationship of interest, three categories of plots were made for all nine filter states. Each category holds two of the three environmental and varies the third in a given plot. The first category of plots varied the trajectory shape. Fig. 4.1 shows an example comparing the different trajectory shapes for an altitude of 412 meters using ALD 5 for the north position. Next, the second category of plots varied the altitude. Fig. 4.2 shows an example comparing the different altitudes for a straight-line trajectory using ALD 5 for the north position. Finally, that leaves the last category to vary the ALD. Fig. 4.3 shows an example comparing the different ALDs for a straight-line trajectory at an altitude of 412 meters. Viewing these types of plots revealed several interesting patterns.

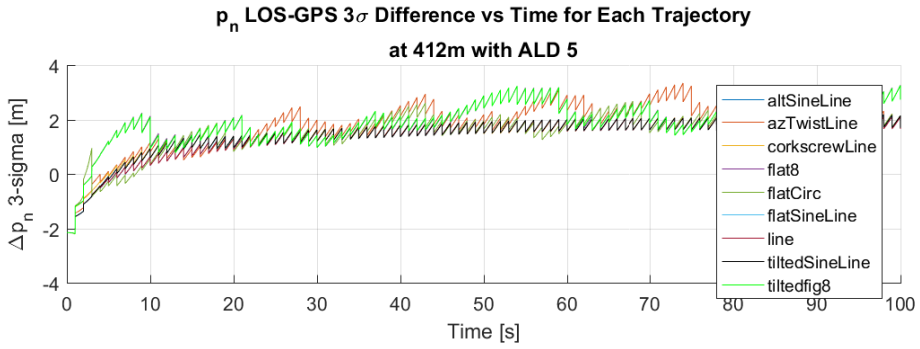

Fig. 4.1: Trajectory shape comparison example of north position

4.2 Summary of Observations

Several patterns were observed in the plots resulting from running all of the trajectory, altitude, and apparent landmark density combinations. The following observations will be discussed in the next section of this chapter.

1. None of the different trajectory shapes tested in this work have any distinguishable effects on filter confidence for any of the estimated states.

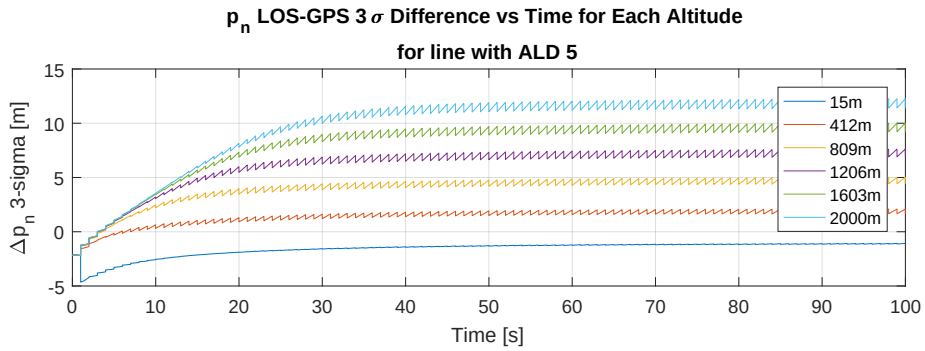

Fig. 4.2: Altitude comparison example of north position

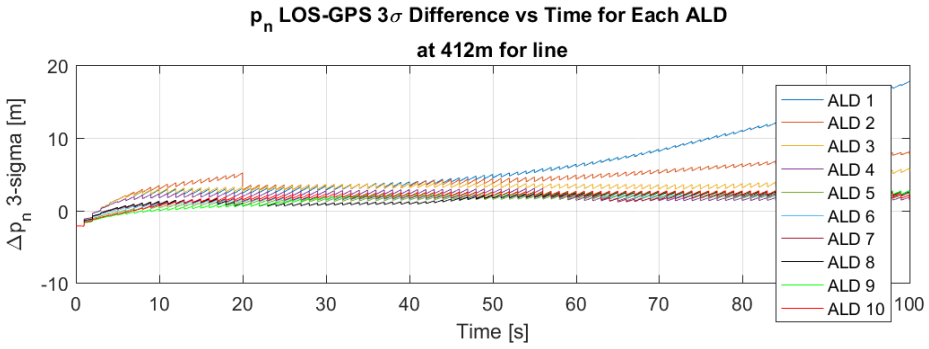

Fig. 4.3: ALD comparison example of north position

2. Attitude confidence is practically the same and is consistently as good as GPS performance.

3. Position confidence generally increases with more measurements towards some maximum knowledge.

4. Position confidence is better when landmarks are observed closer to the edge of the image.

5. Position confidence is increasingly worse at high altitudes.

Following the initial discussion of these observations, a mathematical representation is derived tying together some of the observations about position confidence.

4.3 Initial Analysis of Observations

4.3.1 Trajectory Shapes

The various trajectory shapes included in tests for this work do not have any discernible patterns to suggest a superior trajectory. There are plenty of differences between the results, but all the changes in confidence for each of the trajectories are directly correlated to the number of landmarks observed during the change. There was no evidence of one trajectory shape seeing more or less landmarks than another. This, however, is not a completely conclusive finding. One failing of this experiment is that all of the trajectory shapes were relatively flat and level. None of them had significant variation in pitch or roll. Given the derivation and analysis in section 4.4, it would be interesting to examine results from a trajectory shape with higher pitch and roll angles as part of a future work.

4.3.2 Attitude Confidence

All of the data gathered and examined as part of this work indicated that attitude confidence remained largely unaffected by the changing variables. The only differences can

be partially attributed to relative distance and measurement noise in the form of camera pixel size, though this remains unproved in this work. One interesting finding is related to the vehicle's altitude and how much attitude information is available. Fig. 4.4 shows the roll confidence for all altitudes when flying a straight line using ALD. The most confident scenario is when the vehicle is flying at 15 meters. However, the next highest altitude is the least confident altitude. The confidence appears to get better as the vehicle gets higher for the rest of the altitudes tested. The same pattern appears in all three attitude states.

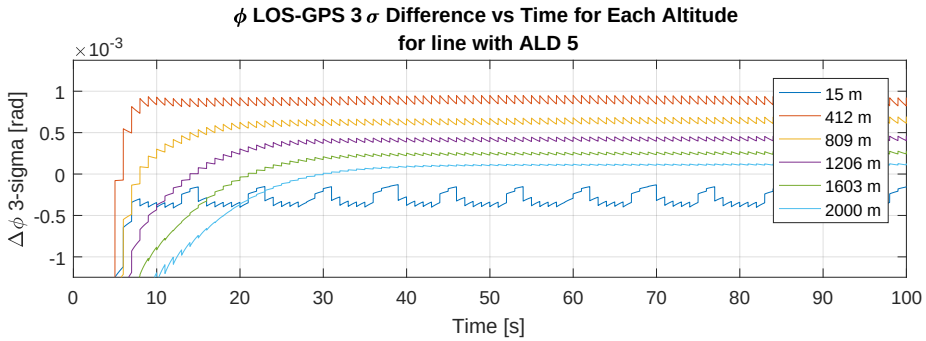

Fig. 4.4: Attitude confidence for the different altitudes

It appears that there is a trade-off between distance from the landmark and the measurement noise. When the landmark is close, the imager is able to capture its position more exactly and the filter understands this. However, at smaller distances, small rotations can appear similar to small translations to the camera. The filter would have a difficult time telling those apart. As distance increases, this effect becomes less apparent.

Although this is an interesting exercise, the effects described here are small (see scale of the plot in Fig. 4.4). Due to its relatively small impact, the concepts observed here are secondary to those in the following section. The proof is therefore left for future work.

4.3.3 Position Confidence and Apparent Landmark Density

Examining ALD-varying plots such as Fig. 4.5 consistently reveals a correlation between the number of landmarks observed and the level of position confidence. The top

plot in the figure shows the position confidence in the north direction for a straight-line trajectory at 2,000 meters. The bottom figure shows the number of landmarks matched for each ALD. There appears to be a general trend here and in several other altitudes where more landmarks imply more knowledge.

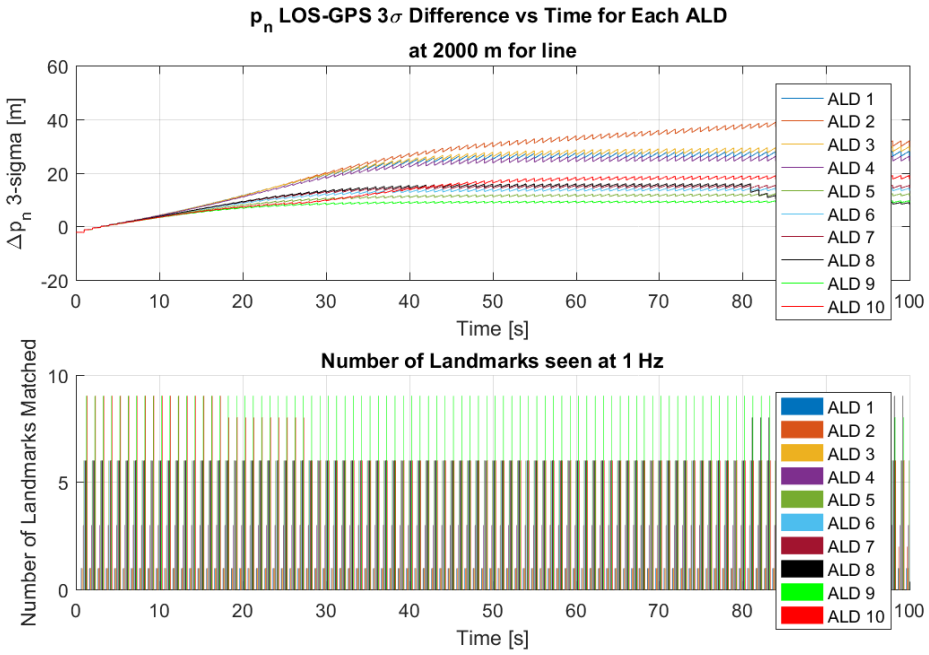

Fig. 4.5: ALD comparison showing increased information for more landmark observations

However, this relationship changes at lower altitudes. Fig. 4.6 shows the same trajectory at 15 meters, but only the first six ALDs are shown. This is because anything that observes three or more landmarks in a given image converges to the same final value. This is true of every other trajectory shape as well as all three position states.

This is an interesting finding because it implies that there is a relationship, at least for low altitudes, where there is a definite number of landmarks that will give maximum amount of navigation knowledge at a given altitude. This work did not collect enough low-altitude trajectory data to explore this further, but ideas regarding this observation are discussed in section 5.2.

Because of this low-altitude observation, the question arises as to whether there is a

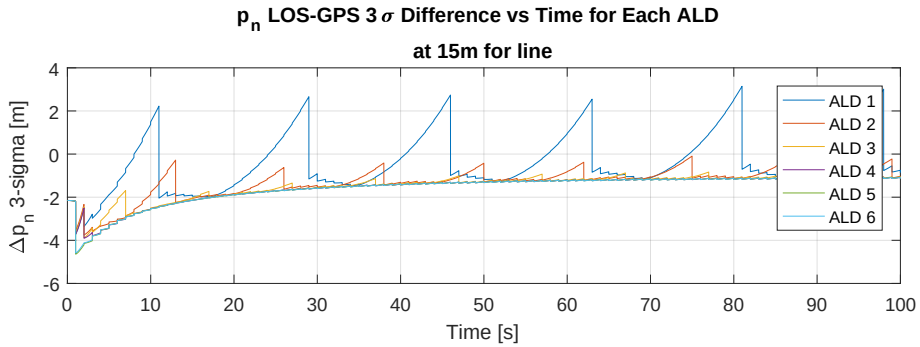

Fig. 4.6: ALD comparison of north position at 15 meters

similar behavior at high altitudes. To explore this further, 30 additional ALDs were created, bringing the total to 40. Two trajectories were run at each altitude above 15 meters (since the 15 meter case had proven to converge) and both showed similar trends. Fig. 4.7 show this trend by plotting the north position results of running the altitude-varying sinusoidal line at 2,000 meters against all 40 ALDs. The legend was omitted from this plot due to its size. The general trend holds true: more landmarks mean more certainty, though each additional landmark adds less information than the ones before it.

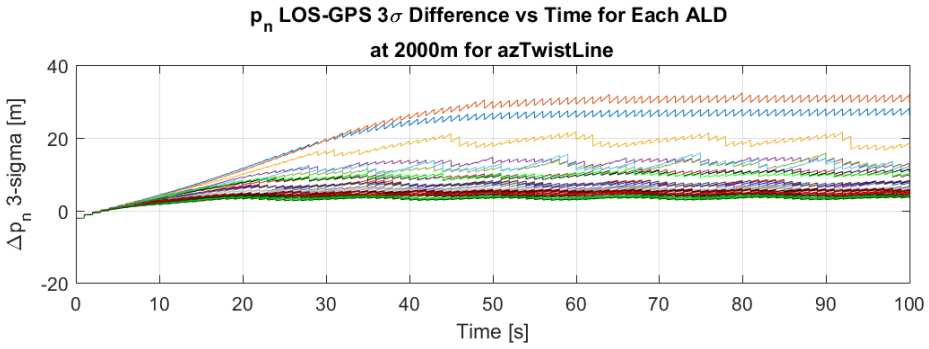

Fig. 4.7: 40 ALDs comparison of north position

This trend is also present at the other altitudes. To better understand how much information is added by each successive measurement, a time slice was taken at 60 seconds of Fig. 4.7 along with the other altitudes down to and including 412 meters. This results in a 3σ difference value for each ALD at the 60 second mark of the run. This was done for

all three position states at each altitude and the results are shown in Fig. 4.8. The number of observed landmarks is included in the bottom plot to show that a nearly linear increase in landmarks observed yields a curve for each altitude that appears to be converging to a final value.

One detail to recall here is that each landmark distribution is laid out in a uniform grid to maximize the measurement information from each camera image. Because of this detail, this empirical data may be a close representation of an ideal curve describing the relationship between altitude and information gained by each successive landmark. Each curve is also approaching zero. The way that this data is shown, this means that the LOS solution is approaching the confidence of a GPS-aided solution.

4.3.4 Position Confidence and Line-of-Sight Angles

Another consistent pattern appears in the position uncertainty plots. On the surface, it appears that a higher apparent landmark density can give less information than a lower apparent landmark density. This first appeared in plots like the one in Fig. 4.9, which has had all other ALD lines removed for clarity. Both ALDs ended up giving the exact same number of landmark observation throughout each simulation.

Because of the way the landmarks are distributed, landmarks observed in these simulations likely would have had similar positions. The difference between the two ALDs is that the ALD 6 makes the landmarks appear slightly further away from the edges because they are denser (i.e. physically closer together) than the landmarks in ALD 5. In other words, the difference is in the measurement geometry of the problem. What is the best measurement geometry? It appears that observations made closer to the edge of the image are better. This makes sense since the measurements are more perpendicular to each other. This is further explained and proved in section 4.4.

4.3.5 Position Confidence and Altitude

The final observation to be discussed in this work is the apparent effect of altitude on position confidence. Every plot that compared results for varying altitudes showed a strong

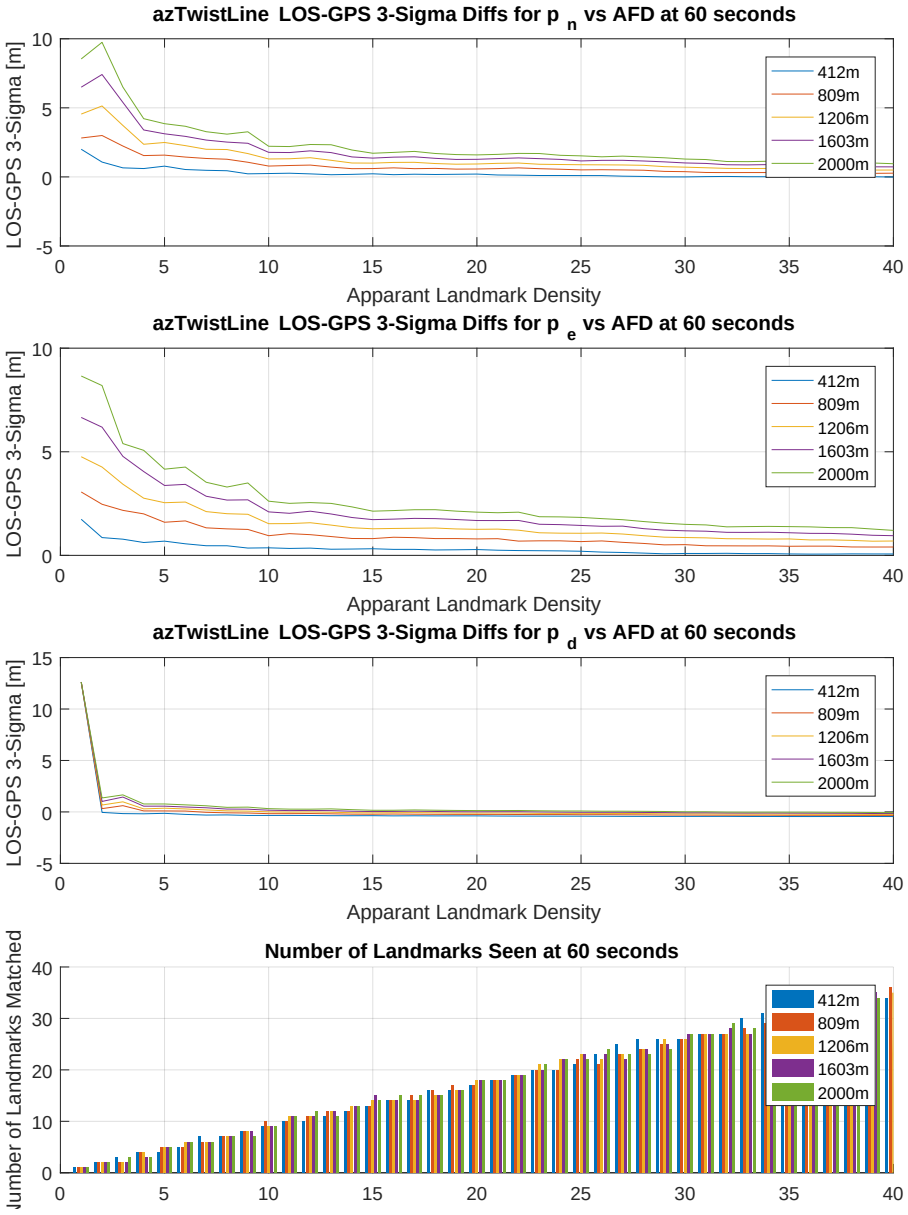

Fig. 4.8: 40 ALDs time-slice comparison of all position states with number of landmarks matched

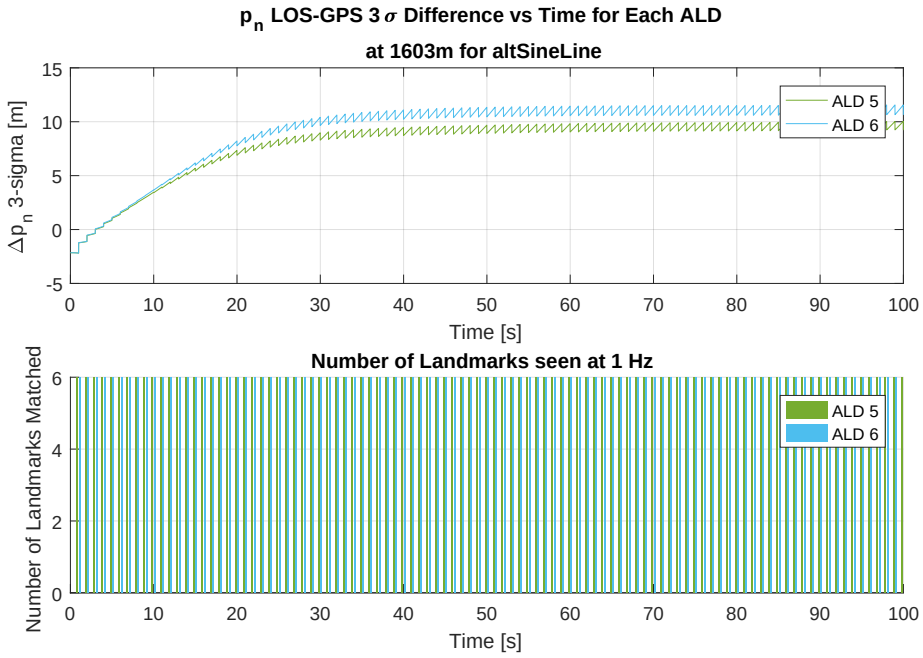

Fig. 4.9: ALD 5 and 6 comparison for north position with number of landmarks matched

similarity to Fig. 4.10. The plot shows results from each of the six altitudes for the line trajectory using ALD 5, but any other altitude comparison plot could have been shown here to similar effect. There is a very clear correlation between altitude and position confidence. Position confidence gets worse as altitude increases.

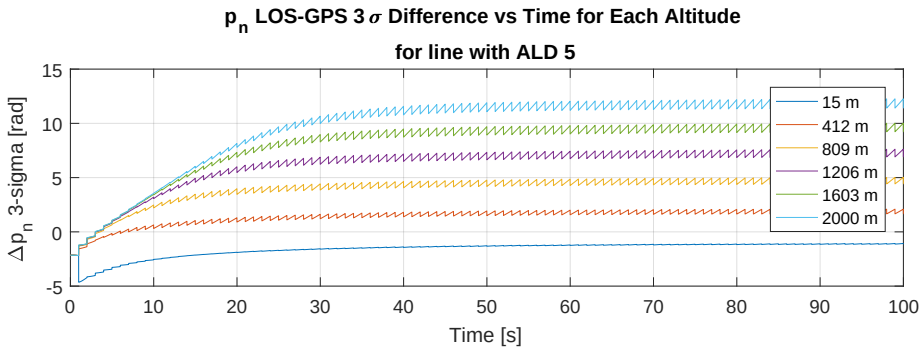

Fig. 4.10: Altitude comparison for a line trajectory using ALD 5

The mathematical proof for this pattern is found in section 4.4 because of its implications in connection to more fully answering sections 4.3.3 and 4.3.4.

4.4 Position Information from LOS Measurements

There is one derivation that supports the observations from above and answers several questions posed by this work regarding the amount of position information obtained from a single LOS measurement: take the trace of the position information matrix, $H_{pos}^T R^{-1} H_{pos}$. This matrix projects the measurement noise into the measurement geometry matrix, resulting in something that tells how much information is in the measurement. This can be better explained by some of the special properties of this matrix.

First, if a matrix is viewed as an organized group of values that stores information, the eigenvectors of a matrix conceptually point in the direction of that information. Eigenvalues, being the magnitude of their corresponding eigenvectors, tell how much information is in those directions. It can therefore be said that the sum of the eigenvalues is a measure of how much information is in a matrix. One special property of matrices is that the sum of the main diagonal terms of a matrix, or trace, is equal to the sum of its eigenvectors. Therefore, the trace of a matrix is conceptually a measure of how much information is in the matrix.

Earlier, the measurement geometry matrix for position, H_{pos}, was defined in 3.98. It is written here for clarity in this derivation:

$$H_{pos} = -\Lambda C_{\mathscr{J}}^{\mathscr{F}} \tag{4.2}$$

Substituting this into $H^T R^{-1} H$ gives

$$H^T R^{-1} H = C_{\mathscr{F}}^{\mathscr{J}} \Lambda^T R^{-1} \Lambda C_{\mathscr{J}}^{\mathscr{F}}. \tag{4.3}$$

This appears to be overly complicated. However, it can be simplified using the principle of eigenvalue decomposition given that the trace of a matrix is equal to the sum of its eigenvalues. Let

$$A = BRB^T \tag{4.4}$$

where A is an $n \times n$ matrix and B is some matrix, D, multiplied by a direction cosine matrix, C, on the left:

$$B = CD. \tag{4.5}$$

Combining these two definitions yields

$$A = CDRD^TC^T. \tag{4.6}$$

Applying eigenvalue decomposition to A would yield

$$A = VEV^T \tag{4.7}$$

where E is the diagonal eigenvalue matrix and V is a rotation matrix comprised of the unit-length eigenvectors of A.

Now, let matrix G be equal to A without its outer rotation matrices:

$$G = DRD^T. \tag{4.8}$$

This implies that

$$A = CGC^T. \tag{4.9}$$

Eigenvalue decomposition of G gives

$$G = WFW^T. \tag{4.10}$$

where W is a rotation matrix comprised of the eigenvectors of G, and F is a diagonal matrix containing the eigenvalues of G. This can then be substituted back into A to yield

$$A = CWFW^TC^T. \tag{4.11}$$

Since C, V, and W are rotation matrices, the following definitions must be true:

$$V = CW, \text{ and} \tag{4.12}$$

$$E = F. \tag{4.13}$$

In other words, the eigenvalues of A are the same as the eigenvalues of G. C therefore changes the eigenvectors, not the eigenvalues. This then implies that the sum of the eigenvalues of A are equal to the sum of the eigenvalues of G. Given that the trace of a matrix is equal to the sum of its eigenvalues, the trace of A must then be equal to the trace of G.

Substituting the original LOS-related matrices into this thinking, it follows that

$$\text{Trace}\left(H^TR^{-1}H\right) = \text{Trace}\left(C^{\mathscr{I}}_{\mathscr{F}}\Lambda^TR^{-1}\Lambda C^{\mathscr{F}}_{\mathscr{I}}\right) \tag{4.14}$$

$$= \text{Trace}\left(\Lambda^TR^{-1}\Lambda\right). \tag{4.15}$$

From here, $\Lambda^TR^{-1}\Lambda$ is expanded using 3.91 to give

$$\Lambda^TR^{-1}\Lambda = \begin{bmatrix} \frac{-\hat{r}^{\mathscr{F}}_{T/\mathscr{F},y}}{\left(\hat{r}^{\mathscr{F}}_{T/\mathscr{F},x}\right)^2} & \frac{-\hat{r}^{\mathscr{F}}_{T/\mathscr{F},z}}{\left(\hat{r}^{\mathscr{F}}_{T/\mathscr{F},x}\right)^2} \\ \frac{1}{\hat{r}^{\mathscr{F}}_{T/\mathscr{F},x}} & 0 \\ 0 & \frac{1}{\hat{r}^{\mathscr{F}}_{T/\mathscr{F},x}} \end{bmatrix} \begin{bmatrix} \frac{1}{\sigma^2_{\delta\lambda_x}} & 0 \\ 0 & \frac{1}{\sigma^2_{\delta\lambda_y}} \end{bmatrix} \begin{bmatrix} \frac{-\hat{r}^{\mathscr{F}}_{T/\mathscr{F},y}}{\left(\hat{r}^{\mathscr{F}}_{T/\mathscr{F},x}\right)^2} & \frac{1}{\hat{r}^{\mathscr{F}}_{T/\mathscr{F},x}} & 0 \\ \frac{-\hat{r}^{\mathscr{F}}_{T/\mathscr{F},z}}{\left(\hat{r}^{\mathscr{F}}_{T/\mathscr{F},x}\right)^2} & 0 & \frac{1}{\hat{r}^{\mathscr{F}}_{T/\mathscr{F},x}} \end{bmatrix} \tag{4.16}$$

$$= \begin{bmatrix} \frac{1}{\sigma^2_{\delta\lambda_x}}\frac{-\hat{r}^{\mathscr{F}}_{T/\mathscr{F},y}}{\left(\hat{r}^{\mathscr{F}}_{T/\mathscr{F},x}\right)^2} & \frac{1}{\sigma^2_{\delta\lambda_y}}\frac{-\hat{r}^{\mathscr{F}}_{T/\mathscr{F},z}}{\left(\hat{r}^{\mathscr{F}}_{T/\mathscr{F},x}\right)^2} \\ \frac{1}{\sigma^2_{\delta\lambda_x}}\frac{1}{\hat{r}^{\mathscr{F}}_{T/\mathscr{F},x}} & 0 \\ 0 & \frac{1}{\sigma^2_{\delta\lambda_y}}\frac{1}{\hat{r}^{\mathscr{F}}_{T/\mathscr{F},x}} \end{bmatrix} \begin{bmatrix} \frac{-\hat{r}^{\mathscr{F}}_{T/\mathscr{F},y}}{\left(\hat{r}^{\mathscr{F}}_{T/\mathscr{F},x}\right)^2} & \frac{1}{\hat{r}^{\mathscr{F}}_{T/\mathscr{F},x}} & 0 \\ \frac{-\hat{r}^{\mathscr{F}}_{T/\mathscr{F},z}}{\left(\hat{r}^{\mathscr{F}}_{T/\mathscr{F},x}\right)^2} & 0 & \frac{1}{\hat{r}^{\mathscr{F}}_{T/\mathscr{F},x}} \end{bmatrix}. \tag{4.17}$$

Since this derivation is aimed at solving for the trace of $\Lambda^TR^{-1}\Lambda$ and the trace is the

sum of the main diagonal elements, only the main diagonal elements are solved for here. If $\Lambda^T R^{-1}\Lambda$ is defined as

$$\Lambda^T R^{-1}\Lambda = \begin{bmatrix} \left(\Lambda^T R^{-1}\Lambda\right)_{11} & \left(\Lambda^T R^{-1}\Lambda\right)_{12} & \left(\Lambda^T R^{-1}\Lambda\right)_{13} \\ \left(\Lambda^T R^{-1}\Lambda\right)_{21} & \left(\Lambda^T R^{-1}\Lambda\right)_{22} & \left(\Lambda^T R^{-1}\Lambda\right)_{23} \\ \left(\Lambda^T R^{-1}\Lambda\right)_{31} & \left(\Lambda^T R^{-1}\Lambda\right)_{32} & \left(\Lambda^T R^{-1}\Lambda\right)_{33} \end{bmatrix}, \tag{4.18}$$

then diagonals are

$$\left(\Lambda^T R^{-1}\Lambda\right)_{11} = \frac{1}{\sigma^2_{\delta\lambda_x}} \left(\frac{-\hat{r}^{\mathscr{F}}_{T/\mathscr{F},y}}{\left(\hat{r}^{\mathscr{F}}_{T/\mathscr{F},x}\right)^2} \right)^2 + \frac{1}{\sigma^2_{\delta\lambda_y}} \left(\frac{-\hat{r}^{\mathscr{F}}_{T/\mathscr{F},z}}{\left(\hat{r}^{\mathscr{F}}_{T/\mathscr{F},x}\right)^2} \right)^2 \tag{4.19}$$

$$\left(\Lambda^T R^{-1}\Lambda\right)_{22} = \frac{1}{\sigma^2_{\delta\lambda_x}} \left(\frac{1}{\hat{r}^{\mathscr{F}}_{T/\mathscr{F},x}} \right)^2 \tag{4.20}$$

$$\left(\Lambda^T R^{-1}\Lambda\right)_{33} = \frac{1}{\sigma^2_{\delta\lambda_x}} \left(\frac{1}{\hat{r}^{\mathscr{F}}_{T/\mathscr{F},x}} \right)^2. \tag{4.21}$$

Finally, the trace of $\Lambda^T R^{-1}\Lambda$ is the sum of these elements.

$$\text{Trace}\left(\Lambda^T R^{-1}\Lambda\right) = \frac{1}{\sigma^2_{\delta\lambda_x}} \left(\frac{-\hat{r}^{\mathscr{F}}_{T/\mathscr{F},y}}{\left(\hat{r}^{\mathscr{F}}_{T/\mathscr{F},x}\right)^2} \right)^2 \tag{4.22}$$

$$+ \frac{1}{\sigma^2_{\delta\lambda_y}} \left(\frac{-\hat{r}^{\mathscr{F}}_{T/\mathscr{F},z}}{\left(\hat{r}^{\mathscr{F}}_{T/\mathscr{F},x}\right)^2} \right)^2 \tag{4.23}$$

$$+ \frac{1}{\sigma^2_{\delta\lambda_x}} \left(\frac{1}{\hat{r}^{\mathscr{F}}_{T/\mathscr{F},x}} \right)^2 \tag{4.24}$$

$$+ \frac{1}{\sigma^2_{\delta\lambda_x}} \left(\frac{1}{\hat{r}^{\mathscr{F}}_{T/\mathscr{F},x}} \right)^2. \tag{4.25}$$

At this point, it is appropriate to assume that in a given camera, the measurement noise will likely be very similar or the same in both directions. This means that $\frac{1}{\sigma^2_{\delta\lambda_x}} = \frac{1}{\sigma^2_{\delta\lambda_y}} = \frac{1}{\sigma^2_{\delta\lambda}}$.

This allows the equation to be simplified to

$$\text{Trace}\left(\Lambda^T R^{-1}\Lambda\right) = \frac{1}{\sigma_{\delta\lambda}^2}\left(\frac{2}{\left(\hat{r}^{\mathscr{F}}_{T/\mathscr{F},x}\right)^2} + \frac{\left(-\hat{r}^{\mathscr{F}}_{T/\mathscr{F},y}\right)^2}{\left(\hat{r}^{\mathscr{F}}_{T/\mathscr{F},x}\right)^4} + \frac{\left(-\hat{r}^{\mathscr{F}}_{T/\mathscr{F},z}\right)^2}{\left(\hat{r}^{\mathscr{F}}_{T/\mathscr{F},x}\right)^4}\right). \tag{4.26}$$

Note that $\hat{\bar{r}}^{\mathscr{F}}_{T/\mathscr{F}}$ is the relative position vector of the observed landmark with respect to the vehicle expressed in the $\mathscr{F}$-frame. This equation can be expressed in terms of relative distance as

$$\text{Trace}\left(\Lambda^T R^{-1}\Lambda\right) = \frac{1}{\sigma_{\delta\lambda}^2}\left(\frac{2}{\left(\hat{r}^{\mathscr{F}}_{T/\mathscr{F},x}\right)^2} + \frac{\left(-\hat{r}^{\mathscr{F}}_{T/\mathscr{F},y}\right)^2}{\left(\hat{r}^{\mathscr{F}}_{T/\mathscr{F},x}\right)^4} + \frac{\left(-\hat{r}^{\mathscr{F}}_{T/\mathscr{F},z}\right)^2}{\left(\hat{r}^{\mathscr{F}}_{T/\mathscr{F},x}\right)^4}\right) \tag{4.27}$$

$$= \frac{1}{\sigma_{\delta\lambda}^2}\left(\frac{2\left(\hat{r}^{\mathscr{F}}_{T/\mathscr{F},x}\right)^2 + \left(-\hat{r}^{\mathscr{F}}_{T/\mathscr{F},y}\right)^2 + \left(-\hat{r}^{\mathscr{F}}_{T/\mathscr{F},z}\right)^2}{\left(\hat{r}^{\mathscr{F}}_{T/\mathscr{F},x}\right)^4}\right) \tag{4.28}$$

$$= \frac{1}{\sigma_{\delta\lambda}^2}\left(\frac{\hat{r}^{\mathscr{F}}_{T/\mathscr{F},x} + d^2}{\left(\hat{r}^{\mathscr{F}}_{T/\mathscr{F},x}\right)^4}\right) \tag{4.29}$$

where d is the relative distance to the landmark.

The values of this vector when expressed in the $\mathscr{F}$-frame are harder to understand from an outside, inertial perspective because it is not expressed in inertially defined terms. Questions mentioned earlier seek to understand the relationship between LOS measurements and position state confidence. To more directly answer this question, the expression for $\text{Trace}\left(H^T R^{-1} H\right)$ should be expressed in terms of $\hat{\bar{r}}^{\mathscr{I}}_{T/\mathscr{F}}$ (the relative position of the landmark with respect to the camera expressed in the $\mathscr{I}$-frame). This would express the result in relative north, east, and downward components. Expressing it this way gives more complete insight into questions brought up in sections 4.3.3 and 4.3.4.

Recalling that

$$\begin{bmatrix} c_{11} & c_{12} & c_{13} \\ c_{21} & c_{22} & c_{23} \\ c_{31} & c_{32} & c_{33} \end{bmatrix} = \begin{bmatrix} c\theta c\psi & c\theta s\psi & -s\theta \\ s\phi s\theta c\psi - c\phi s\psi & s\phi s\theta s\psi + c\phi c\psi & s\phi c\theta \\ c\phi s\theta c\psi + s\phi s\psi & c\phi s\theta s\psi - s\phi c\psi & c\phi c\theta \end{bmatrix} \tag{4.30}$$

from 3.18, $\hat{\bar{r}}^{\mathscr{F}}_{T/\mathscr{F}}$ can be written out as

$$\hat{\bar{r}}^{\mathscr{F}}_{T/\mathscr{F}} = C^{\mathscr{F}}_{\mathscr{B}} \hat{C}^{\mathscr{B}}_{\mathscr{V}} C^{\mathscr{V}}_{\mathscr{I}} \hat{\bar{r}}^{\mathscr{I}}_{T/\mathscr{F}} \tag{4.31}$$

$$= \begin{bmatrix} 0 & 0 & 1 \\ 0 & 1 & 0 \\ -1 & 0 & 0 \end{bmatrix} \begin{bmatrix} c_{11} & c_{12} & c_{13} \\ c_{21} & c_{22} & c_{23} \\ c_{31} & c_{32} & c_{33} \end{bmatrix} \begin{bmatrix} 1 & 0 & 0 \\ 0 & 1 & 0 \\ 0 & 0 & 1 \end{bmatrix} \hat{\bar{r}}^{\mathscr{I}}_{T/\mathscr{F}} \tag{4.32}$$

$$\begin{bmatrix} \hat{r}^{\mathscr{F}}_{T/\mathscr{F},x} \\ \hat{r}^{\mathscr{F}}_{T/\mathscr{F},y} \\ \hat{r}^{\mathscr{F}}_{T/\mathscr{F},z} \end{bmatrix} = \begin{bmatrix} c_{31} & c_{32} & c_{33} \\ c_{21} & c_{22} & c_{23} \\ -c_{11} & -c_{12} & -c_{13} \end{bmatrix} \begin{bmatrix} \hat{r}^{\mathscr{I}}_{T/\mathscr{F},n} \\ \hat{r}^{\mathscr{I}}_{T/\mathscr{F},e} \\ \hat{r}^{\mathscr{I}}_{T/\mathscr{F},d} \end{bmatrix} \tag{4.33}$$

$$= \begin{bmatrix} \left(c_{31}\hat{r}^{\mathscr{I}}_{T/\mathscr{F},n} + c_{32}\hat{r}^{\mathscr{I}}_{T/\mathscr{F},e} + c_{33}\hat{r}^{\mathscr{I}}_{T/\mathscr{F},d}\right) \\ \left(c_{21}\hat{r}^{\mathscr{I}}_{T/\mathscr{F},n} + c_{22}\hat{r}^{\mathscr{I}}_{T/\mathscr{F},e} + c_{23}\hat{r}^{\mathscr{I}}_{T/\mathscr{F},d}\right) \\ \left(-c_{11}\hat{r}^{\mathscr{I}}_{T/\mathscr{F},n} - c_{12}\hat{r}^{\mathscr{I}}_{T/\mathscr{F},e} - c_{13}\hat{r}^{\mathscr{I}}_{T/\mathscr{F},d}\right) \end{bmatrix}. \tag{4.34}$$

Substituting these definitions gives

$$\text{Trace}\left(\Lambda^T R^{-1} \Lambda\right) = \frac{1}{\sigma^2_{\delta\lambda}} \left(\frac{c_{31}\hat{r}^{\mathscr{I}}_{T/\mathscr{F},n} + c_{32}\hat{r}^{\mathscr{I}}_{T/\mathscr{F},e} + c_{33}\hat{r}^{\mathscr{I}}_{T/\mathscr{F},d} + d^2}{\left(c_{31}\hat{r}^{\mathscr{I}}_{T/\mathscr{F},n} + c_{32}\hat{r}^{\mathscr{I}}_{T/\mathscr{F},e} + c_{33}\hat{r}^{\mathscr{I}}_{T/\mathscr{F},d}\right)^4} \right). \tag{4.35}$$

If the attitude of the vehicle is zero, meaning that the vehicle is flying flat, level, and pointing north, then 4.26 is equal to 4.35:

$$\text{Trace}\left(\Lambda^T R^{-1} \Lambda\right) = \frac{1}{\sigma^2_{\delta\lambda}} \left(\frac{\hat{r}^{\mathscr{I}}_{T/\mathscr{F},d} + d^2}{\left(\hat{r}^{\mathscr{I}}_{T/\mathscr{F},d}\right)^4} \right). \tag{4.36}$$

For most flight trajectories, the pitch and roll of the vehicle will be nearly zero. This assumption is consistent with what inadvertently happened creating the observations discussed in section 4.3.1. It explains why similar amounts of information were gained by all of the different trajectories. The attitude of any one trajectory was not different enough from the others to give it either an advantage or disadvantage over the other trajectories.

This derivation appears to contain information that is key to fully explaining the other

observations. 4.36 is likely the central equation to understanding how much information each successive measurement gives. Once this relationship is more completely understood, it is likely that this derivation could also be central to calculating how many landmarks are needed to maximize navigation knowledge at any altitude.

Beyond alluding to information about how many landmarks are needed, it very clearly provides information about where each landmark should be in relation to the vehicle to provide the most position information. This can be interpreted in two ways: where landmarks should be placed along a desired trajectory, or where the vehicle's trajectory should be planned to maximize information available by landmarks that already exist.

Contained in this derivation are proofs for two of the other observations as well. First, it is apparent that, as the vehicle travels closer to a landmark, the navigation system will gain more position information. For a vehicle flying nearly flat and level as is assumed by the final equation, a valid measurement must occur within the sensor's field of view. This limiting factor along with the assumption says that distance from the landmark being measured is dominated by altitude. With these physical boundaries in place, 4.35 is dominated by the altitude in the denominator.

The second observation that can easily be proved is that measurements closer to the edges of the image give more position information. If altitude is kept constant, 4.35 becomes

$$\text{Trace}\left(\Lambda^T R^{-1} \Lambda\right) = \frac{1}{\sigma_{\delta\lambda}^2}\left(\frac{a+d^2}{a^4}\right). \tag{4.37}$$

What this shows is that, if altitude relative to the landmark is kept constant, the distance from the landmark must be increased in the relative north, east, south, or west direction to get more information. This information then is bounded by the sensor's field of view. Maximum position information is therefore observed at the boundaries of the image.

Given the observations and relationships shown in this derivation, these equations clearly have potential to aid in several applications. Some of these ideas are discussed in the final chapter of this work.

4.5 Summary of Findings

The examination of the covariance data from the EKF provided several insights into what design decisions can be used to positively affect image-aided navigation that uses LOS measurements. Several observations are identified above. The quantities varied in this experiment had minimal effect on the filter's attitude confidence. Changing the trajectory shape had no discernible effect. Several patterns were identified in the position uncertainty relating to the number and relative position of observed landmarks.

Most of these patterns connect to one central equation produced by deriving the trace of the position information matrix. The resulting equation and the patterns observed in the data are mutually supportive. Understanding that the trace of the position information matrix gives a measure of the information related to position is a valuable key to better understanding how image-aided navigation using LOS-measurements can be optimized.

CHAPTER 5

Conclusion and Future Work

5.1 Conclusion

In this thesis, sensor data was created using a basic quadrotor model. A continuous-discrete extended Kalman filter then combined it with camera line-of-sight measurements to compute image-aided navigation solutions for various scenarios. Trajectory shapes, altitudes, and apparent landmark densities were each varied and the results were searched for patterns and connecting relationships.

Before this work began, the desired outcome was to produce results that would address three things: to provide some insight into the relationships between trajectory shape, altitude, apparent landmark density, and a vehicle's navigation confidence; to provide a tool for system designs; and to uncover more potential areas of research dealing with the effects of LOS measurements. Accomplishing this would be of worth to the field because it would help to steer research in the direction of better understanding how to maximize information from, and use of, LOS measurements.

The data and analysis presented in this thesis comprise a good start. Several patterns were identified that will be useful to the field of image-aided navigation that have not been formally presented or documented in this context. An equation relating relative landmark location to the amount of information available from the measurement was derived. Both the simplified and general forms of this equation are believed to be potentially useful in several areas of future work to be discussed in the next subsection. And, finally, specific regions of interest in the discussed patterns open the door for new research to better understand different regions of operation.

Image-aided navigation is a quickly expanding solution to the challenges of GPS-denied environments. Though image-aided navigation will not likely replace GPS-aided navigation

as the standard, there is much to learn and improve upon. There were some holes in this research because there was little to no direction as to where to start. Those holes will be filled in as a result of future work.

5.2 Future Work and Relevant Applications

The first suggested future work would be to fill in some of the gaps of this work. There were several questions uncovered as to the relationship between altitude and the number of observations needed to maximize position information. Examining a higher resolution of lower altitude levels would provide valuable insight into this relationship. This is especially important information to have because it is so applicable for the rapidly growing field of small UAVs.

Some interesting applications of this work reside in guidance problems. There is great potential to develop a path planning algorithm similar to work done by Bopardikar et. al., but to use 4.36 as a means to minimize both the covariance and the number of landmarks needed [24].

Another area to apply this equation would be to use it to expand on the landmark placement algorithms developed by Beinhofer et. al. as well as Rathinam and Sharma [20–22]. The idea would be to place the landmarks where they would guarantee maximum position information.

Landmark placement algorithms that utilize the findings of this work would be particularly valuable in urban canyons. There has been general interest in recent years of developing drone delivery services, but GPS signals can be patchy in urban canyons. Using this work's findings to help build up a method of image-aided navigation by placing self-describing landmarks could be a door to the future.

Being able to measure relative position between vehicles in cooperative localization situations is important. Relationships and patterns identified by this work could be applied to these scenarios in order to maximize swarm position knowledge.

On a different line of thinking, one possible expansion to this work could be to explore how more dynamics could be introduced into the system to explore the effects of viewing

landmarks from very different angles. Several systems include a gimbaled camera, which could be used to more easily explore the effects that relative sensor attitude has on position knowledge in measurements.

What is written here is only a small sampling of where the results of this research could be applied and extended. This work hopefully has provided an entry point into better understanding the fundamental relationships between line-of-sight measurements and the variables that affect them the most.

Bibliography

[1] H. B. Christophersen, R. W. Pickell, J. C. Neidhoefer, A. A. Koller, S. K. Kannan, and E. N. Johnson, "A compact guidance, navigation, and control system for unmanned aerial vehicles," *Journal of aerospace computing, information, and communication*, vol. 3, no. 5, pp. 187–213, 2006. [Online]. Available: http://arc.aiaa.org/doi/abs/10.2514/1.18998

[2] J. Wendel, A. Maier, J. Metzger, and G. Trommer, "Comparison of Extended and Sigma-Point Kalman Filters for Tightly Coupled GPS/INS Integration," in *AIAA Guidance, Navigation, and Control Conference and Exhibit*. American Institute of Aeronautics and Astronautics, 2005. [Online]. Available: http://arc.aiaa.org/doi/abs/10.2514/6.2005-6055

[3] R. W. Beard and T. W. McLain, *Small Unmanned Aircraft Theory and Practice*, 1st ed. Princeton University Press, 2012.

[4] W.-W. Kao, "Integration of GPS and dead-reckoning navigation systems," in *Vehicle Navigation and Information Systems Conference, 1991*, vol. 2, Oct. 1991, pp. 635–643.

[5] D. Hoey and P. Benshoof, "Civil GPS Systems and Potential Vulnerabilities," TEST GROUP (46TH) HOLLOMAN AFB NM, TEST GROUP (46TH) HOLLOMAN AFB NM, Tech. Rep., Oct. 2005. [Online]. Available: http://www.dtic.mil/docs/citations/ADA440372

[6] J. R. Rufa and E. M. Atkins, "Unmanned Aircraft System Navigation in the Urban Environment: A Systems Analysis," *Journal of Aerospace Information Systems*, vol. 13, no. 4, pp. 143–160, 2016. [Online]. Available: https://doi.org/10.2514/1.I010280

[7] A. D. Wu, E. N. Johnson, M. Kaess, F. Dellaert, and G. Chowdhary, "Autonomous Flight in GPS-Denied Environments Using Monocular Vision and Inertial Sensors," *Journal of Aerospace Information Systems*, vol. 10, no. 4, pp. 172–186, 2013. [Online]. Available: http://dx.doi.org/10.2514/1.I010023

[8] Y.-M. Ahn, D. J. Block, and R. S. Sreenivas, "Autonomous Navigation and Localization of a Quadrotor in an Indoor Environment," *Journal of Aerospace Information Systems*, vol. 12, no. 12, pp. 699–709, 2015. [Online]. Available: http://dx.doi.org/10.2514/1.I010249

[9] J. Zhang, W. Liu, and Y. Wu, "Novel Technique for Vision-Based UAV Navigation," *IEEE Transactions on Aerospace and Electronic Systems*, vol. 47, no. 4, pp. 2731–2741, Oct. 2011.

[10] P. Sala, R. Sim, A. Shokoufandeh, and S. Dickinson, "Landmark Selection for Vision-Based Navigation," *IEEE Transactions on Robotics*, vol. 22, no. 2, pp. 334–349, Apr. 2006. [Online]. Available: http://ieeexplore.ieee.org/document/1618744/

[11] G. Chowdhary, E. N. Johnson, D. Magree, A. Wu, and A. Shein, "GPS-denied Indoor and Outdoor Monocular Vision Aided Navigation and Control of Unmanned Aircraft," *Journal of Field Robotics*, vol. 30, no. 3, pp. 415–438, 2013. [Online]. Available: http://onlinelibrary.wiley.com/doi/10.1002/rob.21454/full

[12] R. Sharma and D. Pack, "Cooperative Sensor Resource Management to Aid Multi Target Geolocalization Using a Team of Small Fixed-wing Unmanned Aerial Vehicles," in *AIAA Guidance, Navigation, and Control (GNC) Conference*. American Institute of Aeronautics and Astronautics, 2013, dOI: 10.2514/6.2013-4706. [Online]. Available: https://arc.aiaa.org/doi/abs/10.2514/6.2013-4706

[13] M. K. Mohamed, S. Patra, and A. Lanzon, "Designing simple indoor navigation system for UAVs," in *2011 19th Mediterranean Conference on Control Automation (MED)*, Jun. 2011, pp. 1223–1228.

[14] A. Bachrach, S. Prentice, R. He, P. Henry, A. S. Huang, M. Krainin, D. Maturana, D. Fox, and N. Roy, "Estimation, planning, and mapping for autonomous flight using an RGB-D camera in GPS-denied environments," *The International Journal of Robotics Research*, vol. 31, no. 11, pp. 1320–1343, Sep. 2012. [Online]. Available: http://ijr.sagepub.com.dist.lib.usu.edu/content/31/11/1320

[15] D. B. Jourdan and N. Roy, "Optimal Sensor Placement for Agent Localization," in *2006 IEEE/ION Position, Location, And Navigation Symposium*, Apr. 2006, pp. 128–139.

[16] M. P. Vitus and C. J. Tomlin, "Sensor placement for improved robotic navigation," *Robotics: Science and Systems VI*, p. 217, 2011. [Online]. Available: http://www.roboticsproceedings.org/rss06/p28.pdf

[17] T. Wang, "Augmented UAS navigation in GPS denied terrain environments using synthetic vision," Ph.D., Iowa State University, United States – Iowa, 2016. [Online]. Available: https://search-proquest-com.dist.lib.usu.edu/docview/1845054014/abstract/2904121C770949ECPQ/1

[18] J. Zhang, Y. Wu, W. Liu, and X. Chen, "Novel Approach to Position and Orientation Estimation in Vision-Based UAV Navigation," *IEEE Transactions on Aerospace and Electronic Systems*, vol. 46, no. 2, pp. 687–700, Apr. 2010.

[19] R. Sharma, R. W. Beard, C. N. Taylor, and D. Pack, "Bearing-only cooperative geo-localization using unmanned aerial vehicles," in *American Control Conference (ACC), 2012*. IEEE, Jun. 2012, pp. 3883–3888. [Online]. Available: http://ieeexplore.ieee.org/document/6315255/

[20] S. Rathinam and R. Sharma, "A multiple vehicle path covering problem with localization constraints: Formulation and algorithms," in *2015 American Control Conference (ACC)*, Jul. 2015, pp. 3746–3751.

[21] M. Beinhofer, J. Mller, and W. Burgard, "Effective landmark placement for accurate and reliable mobile robot navigation," *Robotics and Autonomous Systems*, vol. 61, no. 10, pp. 1060–1069, Oct. 2013. [Online]. Available: http://linkinghub.elsevier.com/retrieve/pii/S0921889012001418

[22] ——, "Landmark Placement for Accurate Mobile Robot Navigation." in *ECMR*, 2011, pp. 55–60. [Online]. Available: http://aass.oru.se/Agora/ECMR2011/proceedings/papers/ECMR2011_0016.pdf

[23] J. v. d. Berg, P. Abbeel, and K. Goldberg, "LQG-MP: Optimized path planning for robots with motion uncertainty and imperfect state information," *The International Journal of Robotics Research*, vol. 30, no. 7, pp. 895–913, Jun. 2011. [Online]. Available: http://ijr.sagepub.com.dist.lib.usu.edu/content/30/7/895

[24] S. D. Bopardikar, B. Englot, and A. Speranzon, "Multiobjective Path Planning: Localization Constraints and Collision Probability," *IEEE Transactions on Robotics*, vol. 31, no. 3, pp. 562–577, Jun. 2015.

[25] D. C. Brown, "Close-range camera calibration," *Photogrammetric Engineering*, vol. 37, no. 8, pp. 855–866, 1971.

[26] R. Beard, "Quadrotor Dynamics and Control Rev 0.1," *All Faculty Publications*, May 2008. [Online]. Available: http://scholarsarchive.byu.edu/facpub/1325

[27] J. Ferrin, R. Leishman, R. Beard, and T. McLain, "Differential flatness based control of a rotorcraft for aggressive maneuvers," in *Intelligent Robots and Systems (IROS), 2011 IEEE/RSJ International Conference on*. IEEE, Sep. 2011, pp. 2688–2693. [Online]. Available: http://ieeexplore.ieee.org/document/6095098/